Progress in Oceanography 198 (2021) 102685

Contents lists available at ScienceDirect

Progress in Oceanography

journal homepage: www.elsevier.com/locate/pocean

An analysis of Atlantic water in the Arctic Ocean using the Arctic subpolar gyre state estimate and observations

Jeffrey S. Grabon [a], John M. Toole [b,*], An T. Nguyen [c], Richard A. Krishfield [b]

[a] Massachusetts Institute of Technology/Woods Hole Oceanographic Institution Joint Program, United States
[b] Woods Hole Oceanographic Institution, United States
[c] Oden Institute for Computational Engineering and Sciences, University of Texas at Austin, United States

ARTICLE INFO

Keywords:
Arctic ocean
Atlantic water
Ocean circulation
Water properties
Temperature
Ocean state estimate

ABSTRACT

The Atlantic Water (AW) Layer in the Arctic Subpolar gyre sTate Estimate Release 1 (ASTE R1), a data-constrained, regional, medium-resolution coupled ocean-sea ice model, is analyzed for the period 2004–2017 in combination with available hydrographic data. The study, focusing on AW defined as the waters between two bounding isopycnals, examines the time-average, mean seasonal cycle and interannual variability of AW Layer properties and circulation. A surge of AW, marked by rapid increases in mean AW Layer potential temperature and AW Layer thickness, begins two years into the state estimate and traverses the Arctic Ocean along boundary current pathways at a speed of 1–2 cm/s. The surge also alters AW circulation, including a reversal in flow direction along the Lomonosov Ridge, resulting in a new quasi-steady AW circulation from 2010 through the end of the state estimate period. The time-mean AW circulation during this latter time period indicates that a significant amount of AW spreads over the Lomonosov Ridge rather than directly returning along the ridge to Fram Strait. A three-layer depiction of the time-averaged ASTE R1 overturning circulation within the Arctic Ocean reveals that more AW is converted to colder, fresher Surface Layer water than is transformed to Deep and Bottom Water (1.2 Sv vs. 0.4 Sv). ASTE R1 also exhibits an increase in the volume of AW over the study period at a rate of 1.4 Sv, with near compensating decrease in Deep and Bottom Water volume. Observed AW properties compared to ASTE R1 output reveal increasing misfit during the simulated period with the ASTE R1 AW Layer generally being warmer and thicker than in observations.

1. Introduction

The Arctic Ocean, the smallest of Earth's five oceans, may be considered a mediterranean sea since it is nearly enclosed, with inflows and outflows through straits connecting the Arctic with the subpolar oceans. Differences in the water properties of the in- and out-flows manifest the Arctic Ocean water mass transformations associated with the circulation. Inflow from the Pacific Ocean occurs through the Bering Strait between Russia and Alaska and provides relatively fresh water (S ~ 32.5, Coachman and Barnes, 1961). Atlantic inflow, in contrast, is relatively warm and salty (Nansen, 1902). Due to its higher salinity and resulting higher density, Atlantic Water (AW) is found at greater depth than the Pacific Water. Due to its relatively warm temperature, AW is often considered a heat reservoir. Indeed, it has been noted that the stored heat in the AW, if brought to the surface, has the capacity to melt all of the sea ice (e.g. Polyakov, et al., 2017). Less dramatic, an early model study suggested a weak upward ocean diffusive heat flux from the AW of ~2 W/m^2 was required for the Arctic Ocean sea ice cover to remain in long-term steady-state (Maykut and Untersteiner, 1971). The implication is that if the stratification or mixing intensity in the AO were to change such that an enhanced flux AW heat was able to reach the surface, reductions in sea ice would occur. Increasing atmospheric temperatures are understood to be a major cause of sea ice loss (e.g. Overland et al., 2011), but warming AW and its effects have been a recent area of focus (e.g. Polyakov, et al., 2010, 2017; Dmitrenko, 2008). For example, warming in the northern Barents Sea has been linked to decreasing Arctic sea-ice import into the region (Barton et al., 2018), which reduces the freshwater forcing in the Surface Layer, decreases the stratification, and increases vertical heat and salt fluxes from below (Lind et al., 2016). Downstream, the "Atlantification" of the eastern Eurasian Basin, marked by decreased stratification caused by reduced sea ice, a weakened halocline, and shoaling of upper AW depths, has been implicated in increased ventilation and reductions in sea ice (Polyakov, et al., 2017).

* Corresponding author.

https://doi.org/10.1016/j.pocean.2021.102685
Received 9 February 2021; Received in revised form 8 September 2021; Accepted 8 September 2021
Available online 13 September 2021

Inflow from the Atlantic Ocean via the Nordic Seas occurs in two main branches: one traversing the Fram Strait between Svalbard and Greenland and the other passing through the northern Barents Sea as sketched in Fig. 1. Within the Arctic interior, this relatively warm, salty water, called Atlantic Water due to its origin, is often characterized by a local temperature maximum in the vertical. Each AO inflow branch has slightly different characteristics due to their disparate pathways in the Nordic Seas. The Fram Strait AW is around 2.5 °C with a salinity of 34.95 while the inflow of AW from the Barents Sea is around 1 °C and of 34.85 (Rudels et al., 2004). Estimates of the amount of AW each branch contributes to the Arctic Ocean has varied between studies. Time-averaged AW transport estimates from moored arrays in the Fram Strait indicate 3.0 ± 0.2 Sv enters the Arctic Ocean through the Fram Strait in the West Spitsbergen Current (Beszczynska-Moller et al., 2012) while approximately 1.8 Sv of AW is believed to pass through the Barents Sea opening (Skagseth, 2008). Tsubouchi et al. (2012, 2018, 2021) report similar amplitude transports (albeit using different water mass layer definitions) based on inverse modeling of the in- and outflows from the Arctic Ocean as a whole under the constraint of mass conservation. (Direct comparisons of the Tsubouchi et al., 2019 transport estimates with those from an ocean state estimate are discussed here in Section 3).

Deriving from the northern limb of the Atlantic's cyclonic subpolar gyre and the Norwegian Atlantic Current (Andersson et al., 2011), AW is in contact with the surface as it enters the Arctic Ocean via Fram Strait and the Barents Sea. AW in these regions is consequently directly influenced by interactions with the overlying atmosphere and sea ice that cool and freshen the AW as it begins its complex, convoluted traverse through the Arctic. While a portion of the inflow recirculates near Fram Strait (Hattermann, 2016), a significant fraction of the inflow through Fram Strait turns east upon entering the Arctic Ocean to form a boundary current along the continental slope. The Barents Sea branch of AW inflow has lower salinity than the Fram Strait branch, due in part runoff from the Norwegian coast and sea ice melt in the northern Barents Sea. In comparison to the Fram Strait branch, the Barents Sea branch experiences comparatively more cooling due to winter convection over shallower bathymetry (Rudels et al., 1999; Lind et al., 2016; Aksenov et al., 2010).

The Fram Strait and Barents Sea AW branches meet in the St. Anna Trough north of the Barents Sea. This convergence displaces the Fram Strait Branch offshore from the Barents Sea Branch. The two waters interleave as the less saline, cooler Barents Sea Branch overlies the Fram Strait Branch (Rudels et al., 2004, 1999). In the Laptev Sea, freshwater runoff from the Eurasian continent overruns the AW and occupies the upper portion of the water column (the Surface Layer). This freshwater input increases stratification and inhibits winter convection in the Polar Mixed Layer from reaching the depths of the AW. With increasing distance from the Arctic Ocean inflow passages, the AW temperature maximum deepens to 200–400 m. Thus, the AW becomes largely insulated from the atmosphere, leaving mixing and stirring as the principal mechanisms by which AW interacts with adjacent water layers).

The boundary current that distributes AW throughout the Arctic Ocean has been inferred to remain adjacent to the continental shelf as it traverses cyclonically (counter-clockwise) around the Arctic Ocean with several bifurcations (Aksenov et al., 2011; Mauritzen et al., 2013; Rudels et al., 1999). At the Nansen-Gakkel Ridge, it is thought that some AW, primarily from Fram Strait, returns along the ridge (Anderson et al., 1989). Other studies question the existence of a return flow along this ridge due to the absence of a warm AW core at the bathymetric feature and instead, postulate that heat is spread into the Nansen Basin interior by intrusive double-diffusive convection starting at Fram Strait (Swift et al., 1997, Steele and Boyd, 1998). A bifurcation at the Lomonosov Ridge is thought to produce a return flow of AW along the ridge directed toward Greenland (Woodgate, et al., 2001), which in turn contributes heat to the interior of the Amundsen Basin, while the balance of AW is believed to continue along the continental slope into the Makarov Basin.

While the temporal and spatial coverage of observations in the Arctic has increased due to advanced engineering and technology, data density remains sparse, limiting ability to quantify the AW watermass properties and circulation. Numerical models are therefore necessary to fill observational gaps and in addition, can offer insights into circulation and transport pathways. A state-of-the-art coupled ocean-sea ice state estimate, the Arctic Subpolar gyre sTate Estimate (ASTE), uses the governing equations in a numerical model in combination with observations to constrain its parameters to create a best-estimate of the Arctic ocean-sea ice state for the period 2002–2017. This study will analyze the AW Layer in ASTE Release 1 (ASTE R1) to investigate its time-averaged circulation and temporal variation across the Arctic Ocean. While ASTE R1 uses observations to develop a physically consistent circulation, the solution can still exhibit temporal and spatial disagreements with the same and independent observations due to various limitations (Nguyen

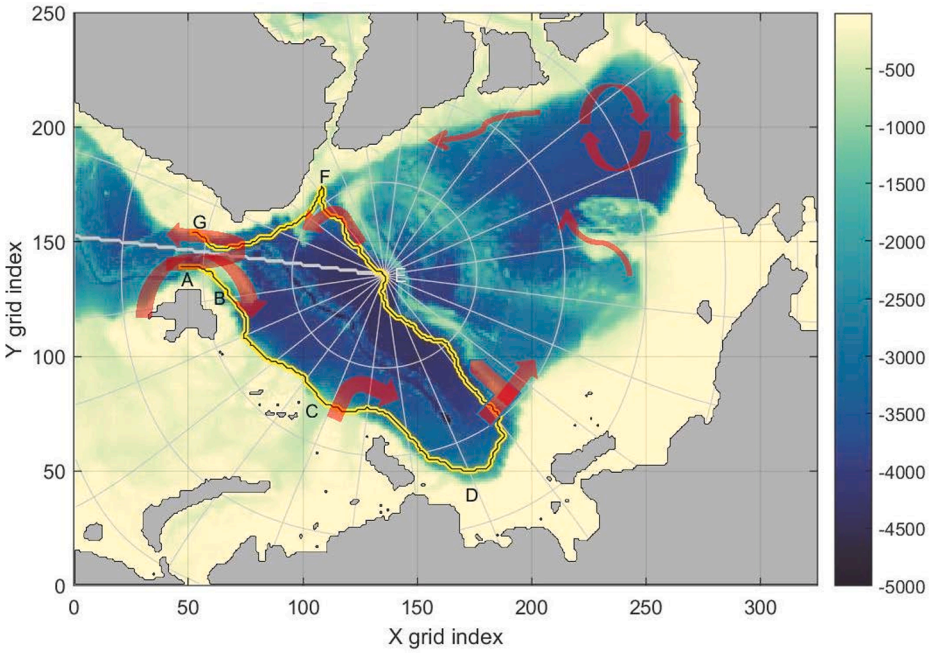

Fig. 1. Bathymetry of the Arctic Ocean sector of the Arctic Subpolar gyre sTate Estimate (ASTE). Depths in meters are displayed on a model grid coordinate system extracted from the full model domain. Latitude circles are drawn at 5-degree increment and meridians at 15-degree interval; the prime meridian is shown with a thicker line. Some elements of the Atlantic Water circulation within the Arctic inferred by Rudels et al., (2012) are superimposed. Also shown is a contour (with letter codes assigned at key locations) used in this analysis to explore propagating AW anomalies. The contour originates in Fram Strait (Location A), extends clockwise along the continental slope andf then parallel to the Lomonosov Ridge to Greenland before exiting at Fram Strait (Location G) The color palette employed in this figure (and several following) was taken from Thyng et al. (2016).

et al., 2021). Thus, this study will also document AW differences between observations and ASTE R1 to further the understanding of where model adjustments may be needed.

Descriptions of the data, model output and computational methods utilized in this investigation are provided in Section 2 below. The significant results of this study are presented in Section 3, followed by a discussion of how this research contributes to the broader scope of the Arctic Ocean and global ocean circulation, including suggestions for future work that builds on these conclusions.

2. Model, data, and computational methods

Monthly mean ASTE R1 output are analyzed in this study to better understand the Arctic Ocean circulation and the processes influencing the AW Layer. ASTE is a regional, medium-resolution coupled ocean-sea ice state estimate, obtained using the Estimation of the Circulation and Climate of the Ocean (ECCO) state estimation framework (Nguyen et al., 2021). The ocean component of ASTE is based on the Massachusetts Institute of Technology General Circulation Model (MITgcm: Marshall et al., 1997). Dynamics and thermodynamics of sea ice are simulated using the MITgcm's sea ice package (Menemenlis, 2005; Losch, 2010; Heimbach, 2010). ASTE employs a latitude-longitude-polar-cap (LLC) grid, specifically LLC-270, with a horizontal resolution of approximately 14 km in the Arctic. In relationship to estimates of the Rossby radius (Nurser and Bacon, 2014; Zhao et al., 2014), ASTE is marginally eddy permitting in the deep Arctic basins but is not eddy resolving near shallower bathymetry. The model domain covers the entire Arctic, Canadian Arctic Archipelago, all adjacent seas (Bering, Kara, Barents, Greenland-Iceland-Norwegian, and Labrador), and the entire North Atlantic. Open boundaries exist at 32.5°S in the Atlantic, 47.5°N in the Pacific and at the Strait of Gibraltar. Conditions at these open boundaries are taken from ECCOv4r3 (Forget et al., 2015; Fukumori et al. 2018; https://ecco-group.org/products.htm). Vertically, ASTE is composed of 50 unevenly spaced levels with the thinnest layers (10 m) at the surface and the thickest (500 m) at 5000 m. The bathymetry is a merged product utilizing the International Bathymetric Chart of the Arctic Ocean (IBCAO; Jakobsson, 2012) for areas poleward of 60°N and Smith and Sandwell version 14.1 (Smith and Sandwell, 1997) south of 60°N, with a blending of these two sources within 100 km of 60°N. Depths of geographic features such as Barrow Canyon, Florida Straits, the Greenland-Iceland-Faroe-Scotland Ridge, gaps between the Aleutian Islands, and the Strait of Gibraltar were adjusted as needed to be consistent with observed depths and ensure consistency of transports and circulations in the state estimate with observations.

Initial estimates of the surface forcing come from the adjusted 3-hourly Japanese Reanalysis (JRA-55) product (Kobayashi et al., 2015). Freshwater fluxes from estuaries were taken from the Regional, Electronic, Hydrographic Data Network for the Arctic Region (R-ArcticNET; Lammers, 2001; Shiklomanov, 2006). Initial conditions were derived from a data-constrained spin-up, that utilized the Pan-Arctic Ice Ocean Modeling and Assimilation System (PIOMAS: Zhang and Rothrock, 2003) sea ice conditions for January 2002 and the (now-superseded) World Ocean Atlas 2013 version 1 (https://www.nodc.noaa.gov/OC5/woa13/) as initial hydrography. Horizontal stirring fields (expressed as isopycnal diffusivities and bolus velocities) and vertical diffusion coefficients (time invariant) were optimized from initial values documented in published literature as specified in Nguyen et al. (2021). In general, only modest departures from initially specified diffusivities resulted (see Nguyen et al. 2021 for details).

Data constraints applied in ASTE R1 include a full suite of satellite and in situ observations from the ECCOv4r3 database (sea surface temperature, sea level anomalies, mean dynamic topography, Argo float and ship-based CTD profiles, moorings; Forget et al., 2015; Fukumori et al., 2018). In addition, for high latitudes, satellite-derived sea ice thickness and concentration data, in situ hydrographic measurements from Ice-Tethered Profilers and ship-based CTDs, and mooring observations at important gateways are used. A full list of observations is provided in Nguyen et al. (2021).

ASTE is fit to observations through a gradient-based iterative least-square minimization of the model-data misfit that considers data and model uncertainties (Nguyen et al., 2021; Wunsch and Heimbach, 2007). In addition, using the method of Lagrange Multipliers, the underlying model physics are strictly enforced. By strictly obeying the conservation laws of momentum and tracers, ASTE is physically consistent and can be used for circulation and budget analyses as there are no artificial fluxes or unaccounted artificial nudging terms. The optimization period of ASTE R1 is January 2002 through December 2017.

Uncertain model input parameters and forcing fields are adjusted during optimization. The ASTE control space is comprised of the initial ocean hydrography, time-independent spatially varying model mixing parameters (horizontal and vertical eddy diffusivities), and the time-varying atmospheric surface forcing. A priori uncertainties based on previously published work ensure that the control space adjustments are within physically reasonable limits (Nguyen et al., 2021). ASTE R1 was obtained after 62 iterations. The optimized controlled input and output fields are publicly available at the UT-Austin ECCO data portal at https://web.corral.tacc.utexas.edu/OceanProjects/ASTE/Release1/ in both NETCDF and raw binary formats.

In this study, monthly mean velocity components at the original C-grid locations were centered to be co-located with the scalar variables (e.g. temperature and salinity) at the grid center locations. The output from January 2002 through December 2017 is concurrent with the observation database for this study. Observations in the Arctic Ocean have been historically limited due to its challenging environment. Autonomous instruments such as Argo floats and AUVs have been developed to collect hydrographic profiles across the world's oceans, but like most ship-based hydrographic observations, these instruments have been generally restricted to ice-free conditions. While some icebreaker and air supported ice camp work has been conducted, sea ice has greatly restricted Arctic Ocean observations. Ice Tethered Profilers (ITPs), developed to operate in the ice-covered environment and obtain hydrographic profiles through the upper ~800 m of the Arctic Ocean, were first deployed in 2004 (Toole et al., 2011; Krishfield et al., 2008). The ITPs yield estimates of ocean temperature and salinity between ~7 and 750 m at 6- to 12-hour interval as the supporting ice floes drift about the Arctic. This study leverages processed in situ ITP data in addition to available ship and ice camp derived CTD profiles obtained during the ASTE R1 analysis period to compare AW Layer properties in observations to ASTE R1 output.

ITP data were acquired from the publicly available archive hosted by the Woods Hole Oceanographic Institution (WHOI; https://www.whoi.edu/page.do?pid=20781). This study uses Level 3 processed data in which sensor corrections are applied, corrupt data are removed, conductivity is calibrated profile-by-profile based on deep water references, outliers are screened, and the data are binned at 1-dbar vertical resolution. Further information regarding the post-processing of ITP data is detailed in "ITP Data Processing Procedures" available on the WHOI ITP webpage. The database examined here contains 49,116 temperature/salinity profiles from a total of 62 ITP systems. ITP data are also available from the National Centers for Environmental Information (NCEI).

Ship and ice-camp CTD data were acquired via the World Ocean Database 2018 archive (WOD18) which is a product of the NCEI and an International Oceanographic Data and Information Exchange (IODE) project. All available CTD profiles poleward of 65°N from 2002 through 2018 were downloaded. CTDs outside the Arctic Ocean between 65°N and 77°N from 112° to 50°E were removed using Ocean Data View (ODV; (Schlitzer, 2020). A total of 15,307 CTD profiles comprise the WOD18 CTD database for this study. Additional CTD profiles were obtained from the Beaufort Gyre Exploration Project that maintains the Beaufort Gyre Observing System (Proshutinsky et al., 2019). Hydrographic profiles collected after 2008 were not included in the WOD18

database query and were therefore separately obtained for this study. This provided 607 additional hydrographic profiles. All of these data were included in the ASTE optimization procedure.

To quantify spatial variations in AW properties, the Arctic Ocean was split into sub-regions using the ASTE bathymetry data, Fig. 2. The Arctic Ocean was first divided into basins using the three main ridges as borders: the Nansen-Gakkel Ridge, the Lomonosov Ridge and the Mendeleyev Ridge. Each Arctic Ocean basin was subsequently partitioned to separately analyze AW properties within the Eurasian and North American sectors of the Arctic. The boundary between the two sides was set along 60°E from 80°N (intersecting Franz Josef Land) to the pole, and along 150°W from the northern coast of Alaska to the pole. The half basins were further subdivided based on water depth and maximum potential density within the water column. The three subsectors are named Shelf, Boundary, and Mid. Shelf sub regions were defined by water depths less than 100 m. Boundary regions were defined to lie within 100 km of the 100 m depth contour or contain profiles with a maximum potential density anomaly relative to 200 dbar of less than 28.9 kg/m^3 in any monthly mean ASTE R1 output. Mid subbasins were the remaining regions more than 100 km from the 100–m depth contour that always contain maximum potential densities greater than or equal to 28.9 kg/m^3 relative to 200 dbar in monthly mean ASTE R1 output.

The entrance and exit of the Arctic Ocean in Fram Strait were defined by mooring locations from the Fram Strait Arctic Outflow Observatory (https://www.npolar.no/en/projects/fram-strait-arctic-outflow-observatory/#toggle-id-1) jointly operated by the Norwegian Polar Institute and the Alfred Wegener Institute. This array is designed to measure inflow from the Atlantic near Svalbard and outflow from the Arctic near Greenland. From Svalbard east to Severnaya Zemlya, 80°N separates the Barents Sea from the Arctic Ocean. On the Pacific side, 70°N was taken as the boundary between the Arctic Ocean and the Subpolar North Pacific. Since the Nansen-Gakkel Ridge bisects Svalbard, the shelf and circumpolar regions of the North American side of the Amundsen Basin were further partitioned into a Svalbard side and Greenland side. The AW which entered the Arctic Ocean near Svalbard is warm and salty while the outflow on the Greenland side is cooler and fresher. To separate the two distinct water types, the regions needed to be split. Similarly, the mid basin for the North American side of the Amundsen Basin was bisected at 81°N to separate the section within Fram Strait, which contains a mix of recirculating AW that just entered the strait and departing transformed Arctic Ocean water, from the rest of the mid basin. The culmination of this Arctic Ocean partitioning is presented in Fig. 2. The shelf regions are not indicated since the AW Layer is at greater depth.

To investigate interannual variations in AW flow and properties along one of the major AW circulation pathways: the Lomonosov Boundary Circuit, a contour was defined adjacent to the continental slope and Lomonosov Ridge, Fig. 1. The contour begins at Fram Strait, turns east north of Svalbard to follow the continental shelf cyclonically through the Laptev Sea, then heads north to parallel the Lomonosov Ridge and extending to the continental shelf offshore of Greenland.

For this study, potential density surfaces are used to define the vertical boundaries the AW Layer and in turn, calculate and analyze the AW Layer properties. Analyses of the ocean observations are based on vertical profiles at 1 dbar vertical resolution. (Those data reported at coarser vertical resolution were linearly interpolated to 1 dbar before analysis.) The two bounding isopycnals: 28.2 kg/m^3 and 28.9 kg/m^3 relative to 200 dbar ($\sigma_{0.2}$), are displayed in Fig. 3 on mean potential density versus potential temperature profiles for regions 10 and 18 (see Fig. 2). These surfaces were selected after studying potential

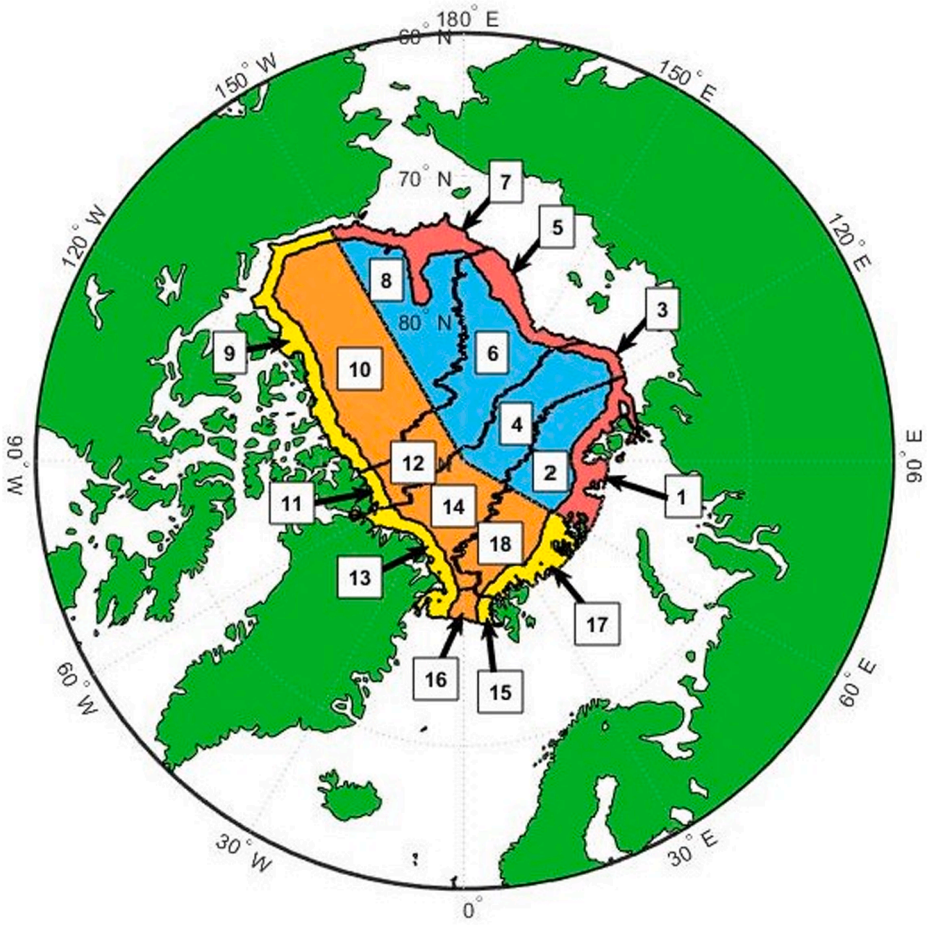

Fig. 2. The Arctic Ocean partitioning scheme developed by Grabon (2020) to examine AW properties. On the Eurasian side of each basin, boundary subbasins are colored red and mid subbasins are blue. On the North American side, boundary subbasins are colored yellow and mid subbasin are orange. The present study focuses on the AW layer properties in the mid subbasins just downstream from Fram Strait (region 18 in the Nansen Basin) and that most distant from this inflow (region 10 in the Canada Basin). For later reference, region 4 lies within the Makarov Basin and region 3 sits at the offshore edge of the Laptev Sea. The border between regions 6–8/10–12 roughly follows the Mendeleyev and Alpha Ridges.

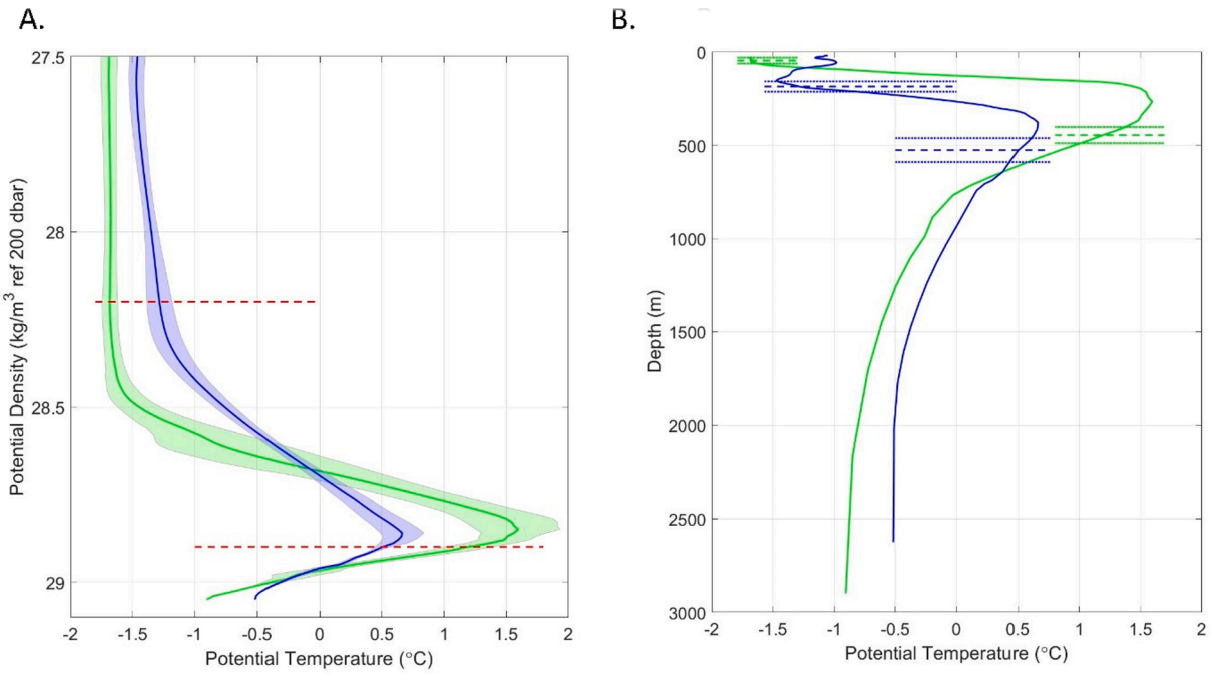

Fig. 3. A) Average profiles of potential temperature versus potential density relative to 200 dbar based on all available Subbasin 18 (green) and Subbasin 10 (blue) with one standard deviation about the mean shaded. The red dashed lines mark the AW bounding isopycnals used in this study. The subbasin regions are shown in Fig. 2. B) The same mean profiles plotted with depth as the vertical coordinate. The mean depths (dashed) and standard deviation (dotted) of the bounding AW isopycnals are plotted in the same color as their associated subbasin profiles.

temperature profiles averaged on a 0.01 kg/m^3 potential density grid using all available observations (CTDs and ITPs) in the database for each subbasin shown in Fig. 2. The choice of 200 dbar for the potential density reference pressure was motivated by the depth of the AW core that is generally observed around this horizon in the Arctic Ocean. The upper AW bounding isopycnal lies below the Pacific Winter Water identifiable in the North American sector of the Arctic Ocean as a potential temperature minimum above the AW Layer temperature maximum (Zhong, et al., 2019). Since ITP sampling is constrained by the length of the tether, the maximum ITP-observed potential density is restricted as well. The lower AW bounding isopycnal was selected to contain approximately 75% of available observations (CTDs and ITPs) in Subbasin 10 where AW is deepest. The bounding isopycnals encompass the AW temperature maximum in the mean observation potential temperature profiles closest and furthest from the areas of AW inflow to the Arctic Ocean. The mean potential temperature profile for the Subbasin 18, which contains AW from both Fram Strait and the Barents Sea, has an AW potential temperature maximum (1.60 °C) at $\sigma_{0.2} = 28.85$ kg/m^3 while the mean Subbasin 10 potential temperature maximum (0.66 °C) occurs at 28.86 kg/m^3. While the maximum temperature of the AW decays with distance from the Arctic Ocean entrances, the temperature on isopycnals above the core is warmer in Subbasin 18 than in Subbasin 10.

The mean profiles displayed with depth as the vertical coordinate rather than potential density, Fig. 3b, document the erosion of the AW heat content from the Nansen Basin to the opposite side of the Arctic Ocean in the Canada Basin. This erosion manifests as an increase in the depth of the temperature maximum with distance from Fram Strait and the Barents Sea. Looking across each subbasin's set of CTD profiles, the depth of the upper bounding isopycnal varies less than the lower, consistent with the vertical structure of the first baroclinic mode in the Arctic (Zhao et al., 2014).

To facilitate comparison with the observed AW characteristics and to explore the state estimate-derived circulation of the layer, monthly-averaged ASTE R1 profiles of potential temperature, salinity and horizontal velocity were linearly interpolated to 1-meter resolution, potential density profiles were derived, and AW layer properties were estimated by averaging/integrating between the same two isopycnals as discussed above. ASTE R1 estimates of AW Layer properties were compared to the observations in each of the subbasins shown in Fig. 2. ASTE R1 monthly-mean AW properties for each subbasin were estimated by averaging output from all gridpoints within each subbasin. For a more direct comparison to observations, model data from the month of each observation at the model grid cell closest to each observation were also examined. Only observations where both AW bounding isopycnals existed within the observed profile and its associated ASTE R1 water column in the monthly mean output were included in this analysis.

An ASTE R1 - based estimate of the AW general circulation was made using the time-averaged model water property and velocity relative to the ASTE grid. The time-averaging spanned January 2010 through December 2017, the period after a surge in AW flow (discussed in Section 3.4 below) occurred in the ASTE R1 output. Following the surge, the model circulation achieves an approximate steady-state, which permits a best analysis of the time-averaged AW Layer flow. The 96 monthly fields of AW Layer properties and horizontal transport (on the ASTE grid, see Fig. 1) from this time interval were averaged. Initial streamfunction estimates on the ASTE grid were then calculated by integrating the x-directed mean layer transport at each model grid cell in the y-direction from Eurasia to North America along each x-line of grid cells. The time averaged ASTE R1 AW circulation is horizontally divergent owing to water mass transformations and interannual trends in water mass layer volumes. In such cases, the transport streamfunction is not formally defined. Therefore, a (non-unique) estimate of the average horizontally non-divergent flow was also derived. At each x-line, an estimated linear transport curve in the y-direction was made from the initial streamfunction estimate. The linear curves began at zero on the Eurasian coast and ended at a value equal to the initial streamfunction on the North American coast. The linear trend was removed so that layer streamfunction values were equal to zero at each coast, thus yielding a realization of the non-divergent component of the flow. This is a non-unique method of deriving the non-divergent component of the AW circulation. The actual model divergent field for the time-mean

circulation is noisy at the grid resolution and practically indistinguishable from the uniform divergent field assumed in constructing the non-divergent circulation. To complement these circulation estimates based on streamfunctions, streamline maps of the AW Layer-averaged flow field were constructed.

The overturning (divergent) component of the time-averaged circulation can be estimated using the full ASTE R1 mean velocity fields integrated over a series of adjoining density layers. The overturning circulation is diagnosed here using three density layers: a Surface Layer (potential densities relative to 200 dbar < 28.2 kg/m^3, the AW Layer, and a Deep and Bottom Water Layer ($\sigma_{0.2} > 28.9$ kg/m^3). The volumes of each of these layers within the Arctic Ocean in ASTE R1, between Fram Strait and the Barents Sea on the Atlantic side and the Bering Strait on the Pacific side were calculated for every month. The rate of volume change for each layer across the entire Arctic Ocean from January 2010 through December 2017 was obtained by subtracting the former volume from the latter volume and dividing by the time interval. Next, the net volume transports into or out of each layer at the Arctic Ocean boundaries (and net precipitation plus runoff minus evaporation) were estimated for each month and the results were averaged. Temporal change in layer storage, the water mass transformations and flows between the layers (across isopycnals) were then inferred through volume conservation. Contributions from river runoff and precipitation minus evaporation in ASTE R1 were included in the Surface Layer budget. The ASTE R1 average sea ice divergence was also calculated and found to not contribute significantly to the Surface Layer volume budget. Not considered in this analysis were the (parameterized) eddy bolus transports into or out of the Arctic Ocean that were judged to be negligible.

3. Results

A myriad of research topics may be explored using the ASTE R1 output, separately or in combination with available observations. This study focuses on four. Section 3.1 examines the fidelity of ASTE R1 estimates of AW layer properties to observations. This is followed by discussions of the time-averaged AW characteristics and Arctic overturning circulation for the period 2010 through 2017 (Section 3.2) and the mean annual cycle of AW inflow and outflow to/from the Arctic Ocean (Section 3.3). The Results section is concluded with an investigation into AW interannual variability seen in ASTE R1 (Section 3.4). Many other avenues of study have and are being pursued, including those that exploit the full ASTE R1 solution to quantify the dynamics governing specific physical processes (e.g. Nguyen et al., 2020, 2021).

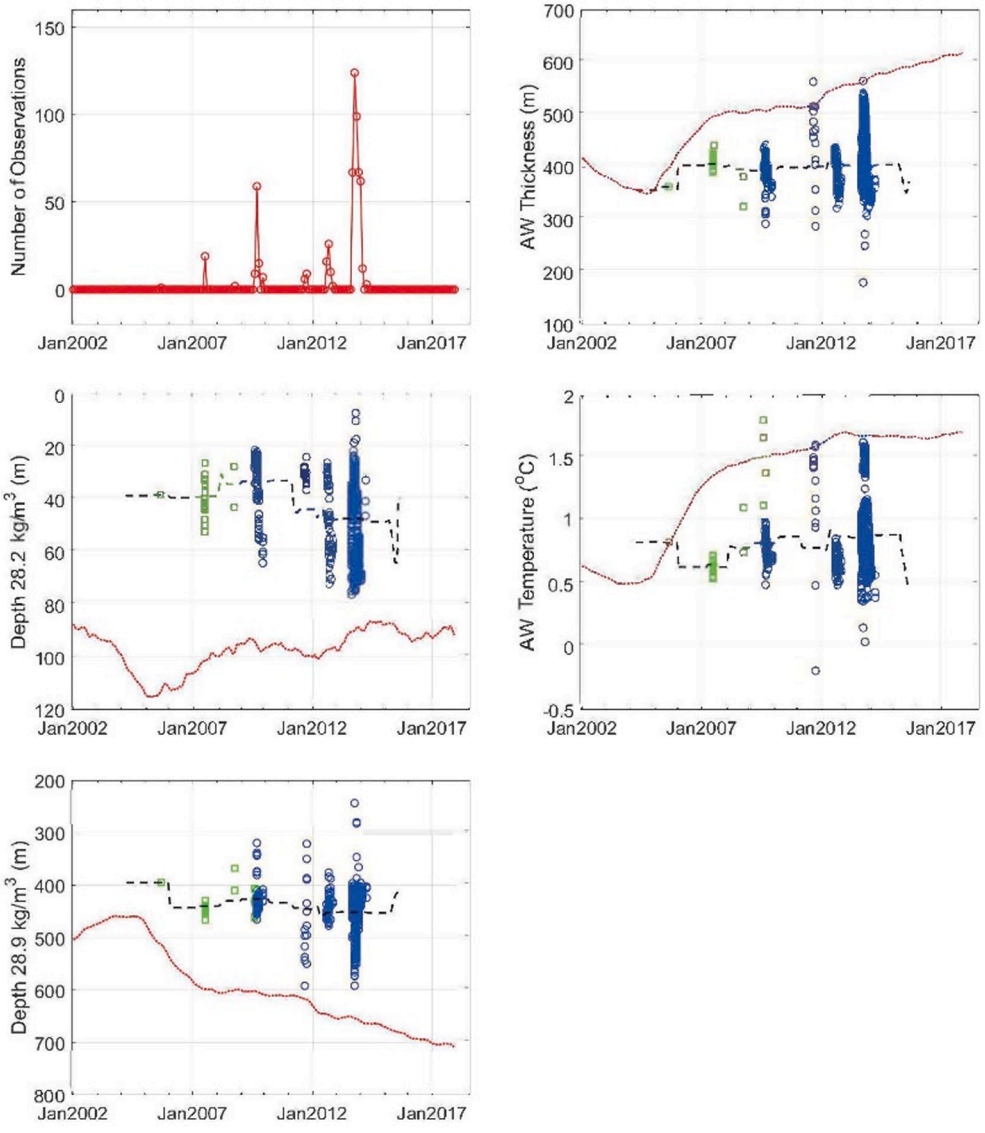

Fig. 4. AW Layer property assessments for Subbasin 18 (see Fig. 3). Left column Top: number of hydrographic observations in the subbasin each month. Middle: depth of the 28.2 kg/m^3 $\sigma_{0.2}$ isopycnal in individual observations (symbols) and derived from ASTE R1 output averaged over all grid points in the subbasin (red curve). Estimates from ITP profiles are shown in green, ship observations in blue. The black dashed curve is a 36-month running average of the observation. Bottom: as above for the 28.9 kg/m^3 $\sigma_{0.2}$ isopycnal. Right column Top: thickness of the AW layer in observations and ASTE R1. Middle: AW Layer averaged potential temperature in observations and ASTE R2. Symbols and curves are as described for the other panels.

3.1. Model-data comparison

ASTE R1 water property fields and circulation are the result of a minimization procedure of a cost function that in part, includes weighted differences between observed and model temperature and salinity estimates on depth surfaces (Nguyen, et al., 2021). Despite a dramatic increase in available upper ocean hydrographic observations in this century, the Arctic remains sparsely observed, particularly in boundary current regions. As a complement to the model misfit diagnostics discussed by Nguyen et al. (2021), compilations of observed and model AW property differences within each Arctic Ocean subbasin were constructed and examined. Results from two regions, Subbasins 10 and 18, are chosen for detailed discussion for the following reasons: Subbasin 18 is near the AW inflow areas and contains AW from both Fram Strait and the Barents Sea. On the opposite side of the Arctic Ocean, Subbasin 10 is furthest from the AW sources. The Mid subbasins were selected since they are larger and contain more observations than their neighboring Boundary regions (See Fig. 2).

Relatively few hydrographic observations are available in Subbasin 18: a total of 615 ITP and CTD water column profiles from the 2002–2017 time period that are biased to the summer season, Fig. 4. The ASTE R1 upper AW bounding isopycnal in this region at the beginning of the state estimate period lies at approximately 90 m depth and increases to 115 m depth by early 2005. Later in time, the isopycnal shoals to return close to its starting level by the end of the analysis period. In comparison, observed 28.2 kg/m^3 isopycnal depths are all shallower than ASTE R1, lying around 40 m in the earliest profiles, increasing to an average depth of around 50 m during 2015. The model misfit decreases with time.

Depth of the lower bounding isopycnal, $\sigma_{0.2} = 28.9$ kg/m^3, the AW Layer thickness and the AW Layer average potential temperature in ASTE R1 follow patterns that are similar to each other. The ASTE R1 subbasin-mean 28.9 kg/m^3 isopycnal descends from approximately 450 m in 2005 to 600 m in 2007, then less rapidly to 700 m by 2017. All of the observed lower isopycnal depths are shallower than the subbasin mean ASTE R1 values. There is a 300 m spread in observed AW bottom bounding isopycnal depths late in 2011 and in 2013 which is not seen in ASTE R1. It is the greater depths of the bottom isopycnal in ASTE R1 compared to observations that result in the AW thickness discrepancies of magnitude 100 m seen in Fig. 4.

Individual estimates of observed Subbasin 18 AW layer-averaged temperature over the analysis period ranged between ~0 °C and ~1.8 °C. The 36-month running mean of observed AW temperature was much more consistent with a maximum to minimum difference of less

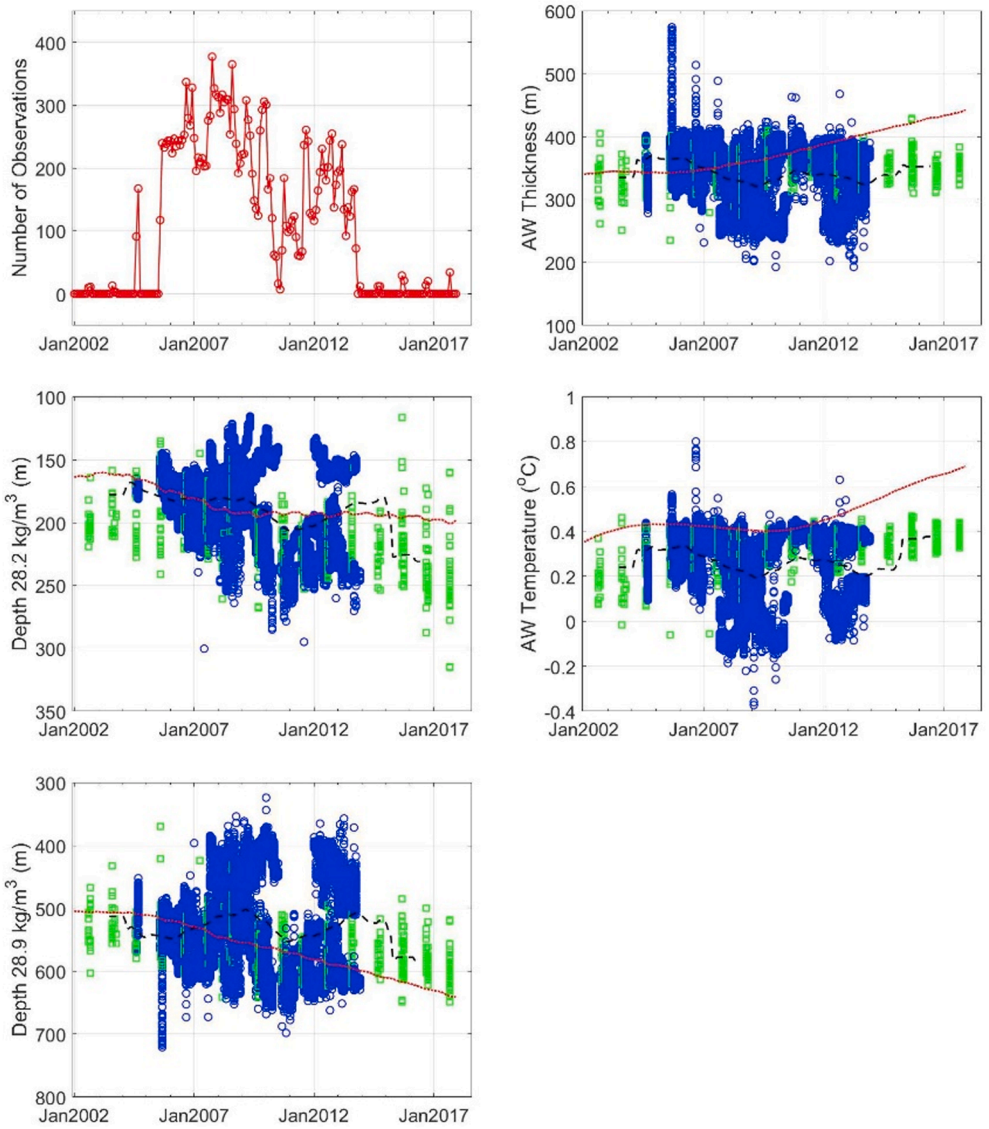

Fig. 5. As in Fig. 4 but for Subbasin #10 (see Fig. 3).

than 0.5 °C. The ASTE R1 output suggests there may be a slight bias in the observations (associated with the spatial distribution of the observations) with the full Subbasin 18 average AW temperature being slightly greater than the running mean of the model estimates at the observation locations (see Grabon, 2020). ASTE R1 layer-average AW potential temperature in Subbasin 18 is seen to increase over the duration of the model output with a subbasin mean near 0.7 °C in 2002 and concluding at 1.7 °C. The fastest increase in model temperature occurs between January 2005 and January 2007 as a surge of AW passes through the region (see Section 3.4). In contrast, the observed layer-averaged AW temperature data do not show the same interannual trend.

The analysis now shifts to Subbasin 10 on the opposite side of the Arctic Ocean. The observational database for this region holds more than 20,000 hydrographic profiles over the analysis period with data more uniformly distributed through the seasons, Fig. 5. The depth of the $\sigma_{0.2} = 28.2$ kg/m^3 isopycnal in this region increased with time in ASTE R1 from approximately 160 m at the beginning of the state estimate period to 200 m by its conclusion. The monotonic increase begins in 2004. A similar trend is seen in the observations, with no significant difference with ASTE R1 in the 36-month running average estimate. This gradual deepening occurs in the subbasin that contains the Beaufort Gyre: a region that has been accumulating freshwater, driven by Ekman convergence (Proshutinsky et al., 2019). This would explain the gradual deepening of the 28.2 kg/m^3 isopycnal.

ASTE R1 depth of the $\sigma_{0.2} = 28.9$ kg/m^3 isopycnal also increases monotonically with time. In January 2002 the area-averaged isopycnal depth is 500 m; it increases to approximately 650 m by December 2017. Observed isopycnal depths also show a (smaller) deepening trend, but with more variability: ~300 m range in isopycnal depth at any given time versus ~100 m in the ASTE R1 estimates at the observation sites (not shown). Some of the variability in the observations is due to eddy motions that are not captured in the medium-spatial-resolution ASTE R1 monthly mean output. The misfit in the lower AW bounding isopycnal depths is the cause for the AW thickness discrepancy.

ASTE R1 AW thickness, that begins the analysis period at 350 m, increased to nearly 450 m by December 2017. On the other hand, the observed AW thickness is steady at around 350 m in the 36-month running mean of the observations. This results in an increasing difference between the model and observations during the state estimate period that begins near zero and ends with ASTE R1 AW thickness some 100 m greater than the observations. Akin to Subbasin 18, Subbasin 10 also shows an increase in AW layer-averaged temperature over the duration of ASTE R1 output, although smaller in magnitude (~0.3 °C vs. ~1 °C) and with warming commencing later (January 2011 vs. January 2005). This warming trend persists through to the end of the state estimate period in December 2017. The decimated ASTE R1 data set with values at the times and locations of the observations is consistent with the true area averages until ~2014, after which there is suggestion of a low bias at the observation sites (Grabon, 2020). Observed AW average temperatures are generally less than the ASTE R1 values for the entire duration of ASTE R1 output. The observations indicate a warming in the subbasin of less than 0.2 °C from 2004 to 2017 in the 36-month running mean.

Despite the ASTE optimization procedure designed to minimize model misfit with observations, differences with observed AW Layer properties are found. Notably, the metrics examined here (AW Layer thickness defined between two bounding isopycnals and layer-averaged temperature) are not explicitly represented in the ASTE optimization cost function (that includes temperature and salinity differences on depth surfaces). Moreover, error is incurred when interpolating and integrating ASTE level model output between isopycnals. Nevertheless, ASTE R1 is judged to be a useful, dynamically self-consistent synthesis of the available observations and as such, was explored to elucidate the character of Atlantic Water in the Arctic Ocean.

3.2. Time-averaged fields: 2010–2017

The ASTE R1 time-averaged distribution of AW Layer potential temperature averaged over the period January 2010 through December 2017 (Fig. 6a) shows that, as expected, the AW is warmest where it enters the Arctic Ocean at Fram Strait with a mean potential temperature of 2.67 °C. Following the generally-accepted AW pathway along the continental shelf north of Svalbard, Franz Josef Land, and the St. Anna Trough, the mean AW Layer potential temperature decreases slightly but generally remains warmer than 2 °C. In the Laptev Sea, the AW Layer temperature falls to approximately 1.5 °C. This cooling is likely due to vertical mixing resulting from atmospheric forcing as well as the lateral influence of cooler shelf water (Rudels et al., 1999; Lenn et al., 2009). The AW remains around 1.5 °C along the Amundsen Basin side of the Lomonosov Ridge up to the pole with some of this heat appearing to spread across the ridge into the Makarov Basin. The coldest mean AW Layer is found in the Canada Basin where temperatures fall below 0.5 °C, reaching a minimum of 0.16 °C in Subbasin 9 close to the continental shelf.

The maximum mean AW thickness (Fig. 6b) of 738 m is located in Subbasin 1 along the continental shelf poleward of Severnaya Zemlya; the minimum mean AW thickness, 194 m, occurs at an isolated location near Franz Josef Land in Subbasin 17. In the Arctic Ocean interior, the AW Layer is thickest following the accepted AW pathway along the continental shelf in the Nansen Basin continuing into the Laptev Sea, and along the Lomonosov Ridge toward the pole. The AW is thinner away from the ridge and shelf. The mean AW Layer thickness is less on the North American side of each subbasin. Lateral variations in AW thickness are related to the geostrophic circulation (discussed below) through the thermal wind balance.

Spatial structure in the mean AW bounding isopycnal depths (Fig. 7) provide additional insight into mechanisms associated with AW Layer thickness variation. Excluding grid points where the upper bounding isopycnal outcropped in one or more months of the analysis period, the minimum mean AW upper isopycnal depth of 35 m is located near Fram Strait in Subbasin 16. A large gradient exists within Fram Strait where the AW inflow near Svalbard lies alongside outgoing AW in the East Greenland Current. Upper AW bounding isopycnal depths generally increase with distance from the AW entrances into the Arctic Ocean. Buoyancy input by Bering Strait inflow, P–E and ice melting in combination with mixing cause the lower AW bounding isopycnal to deepen with distance from Fram Strait. The deepest mean depth of the $\sigma_{0.2} = 28.2$ kg/m^3 surface is located in Subbasin 7 north of the Chukchi shelf where mean Ekman downwelling is associated with the Beaufort atmospheric high-pressure cell. While spatial variations in mean AW Layer thickness mirror geographic features such as the Lomonosov Ridge, the spatial distribution of mean upper isopycnal depth does not. The Lomonosov Ridge is seen as an area of greater mean lower isopycnal depths relative to locations away from the shelves and ridge. Thus, much of the spatial variability in AW thickness which manifested geographic features is due to the spatial variability of the lower bounding isopycnal.

The full, time-averaged transport streamfunction contoured at a 0.25 Sv interval depicts well the AW circulation pathways in ASTE R1, Fig. 8. Recall that in this implementation, the full streamfunction is composed of both the divergent and non-divergent mean flow contributions. Beginning at Fram Strait, 3.9 Sv of AW enters the Arctic Ocean on average. Some of the AW immediately recirculates back through Fram Strait as seen in the streamlines curving back toward Greenland. Approximately 1.8 Sv of AW turns to the right along the continental shelf north of Svalbard, indicating that approximately 2.1 Sv recirculates within Fram Strait. The Barents Sea Branch contributes approximately 1.6 Sv of AW to the Arctic Ocean, the vast majority flowing northeast of Franz Josef Land. This contribution was estimated at multiple model locations: off the coast of Novaya Zemlya and in the St. Anna Trough. Little mean transport of water within this study's AW density class passes between Svalbard and Franz Josef Land; perhaps the Franz

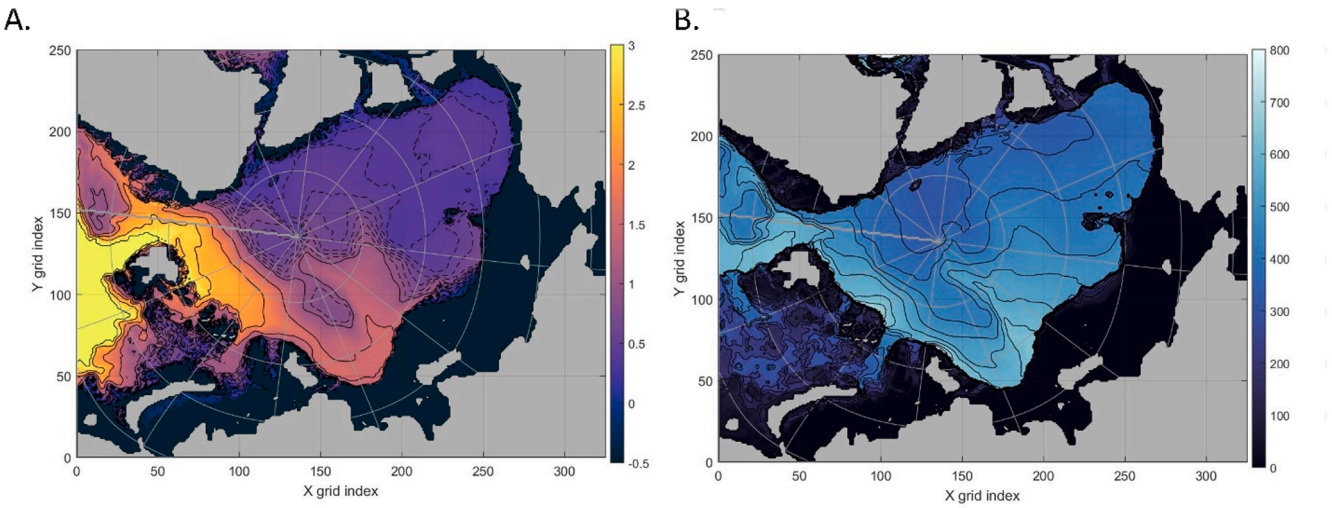

Fig. 6. Time-averaged AW Layer ($\sigma_{0.2}$ between 28.2 and 28.9 kg/m^3) potential temperature (panel a) and layer thickness (panel b) for the period January 2010 through December 2017 in ASTE R1. Areas in black are shallower than the AW layer. Solid contours in panel A are drawn at 0.5 °C increment between 1 and 3 °C with dashed contours at 0.1 °C increment between −0.5 and 1.0 °C. Layer thickness is contoured in panel B at 50 m increments. Black areas are where no water existed between the AW bounding isopycnals. Latitude circles are drawn at 5°interval and meridians at 30°interval.

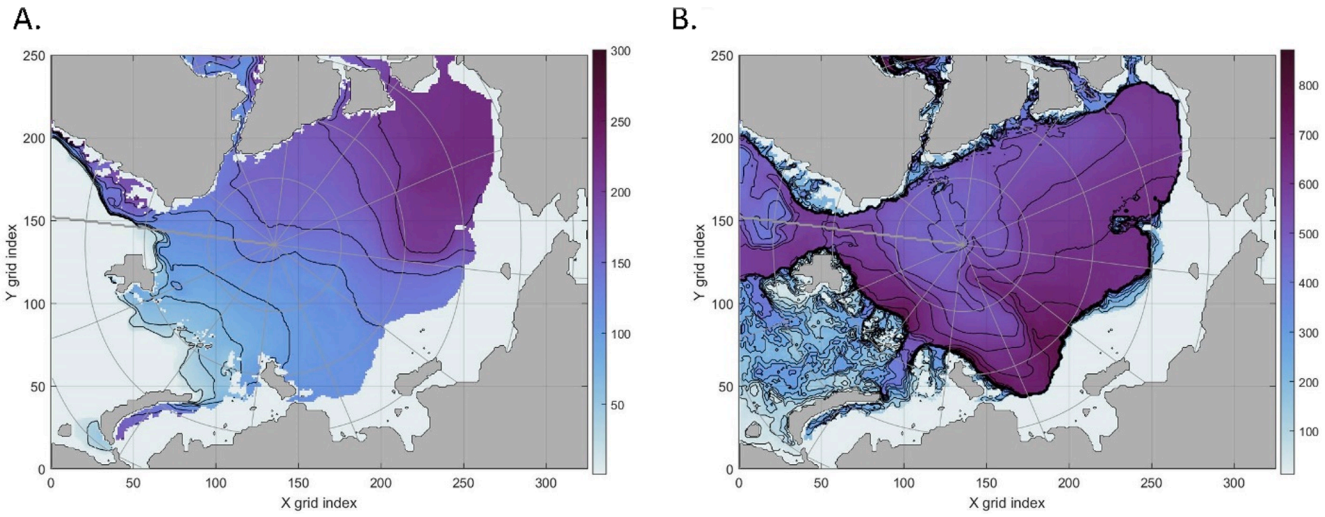

Fig. 7. Time-averaged depth of the $\sigma_{0.2}$ isopycnal 28.2 kg/m^3 (A) and 28.9 kg/m^3 (B) for the period January 2010 through December 2017 in ASTE R1. Areas in pale blue are where the isopycnal did not exist in the time average. The contour interval in panel A is 25 m and in panel B it is 50 m.

Joseph branch of flow in ECCO Version 4 Release 3 output analyzed by Asbjornsen et al. (2020) has lower density. After both inflow branches merge at Severnaya Zemlya, the mean boundary current transport is 2.7 Sv. The AW flows cyclonically into the Laptev Sea with the majority of the flow, 2.4 Sv, turning north along the Lomonosov Ridge, while only 0.5 Sv crosses the ridge adjacent to the shelf to continue as a circumpolar current.

After turning north at the Lomonosov Ridge, 1.2 Sv of AW crosses over the Lomonosov Ridge rather than following the ridge past the Pole. The ASTE R1 time-mean circulation also suggests existence of a cyclonic gyre on the Eurasian side of the ridge near the Laptev Sea with a couple closed streamfunction contours. Another gyre-like recirculation is seen near the Ridge on the North American side of the basin The AW flow that crossed the Lomonosov Ridge enters the Makarov Basin and the Canada Basin before turning toward Fram Strait at the North American shelf north of the Canadian Archipelago. The divergent component of the flow results in transport streamlines appearing to intersect the North American coast. In the Canada Basin, AW flows anticyclonically, in the same direction of the upper ocean in the Beaufort Gyre. Though many forward models show a wide range of AW-layer circulation sense from varied strength cyclonic to weak anti-cyclonic (Holloway et al. 2007; Aksenov et al. 2011), the mechanism controlling the sense of circulation of this layer below the near-surface wind-driven anti-cyclonic Beaufort Gyre circulation remains an active research topic. In a study using forward modeling and focusing on the AW boundary current, Aksenov et al. (2011) showed an eastward flow of AW below a rather weak westward Beaufort Gyre upper ocean flow across ~152°W over the continental slope. The modeling study of Karcher et al. (2007) suggests that the sense of the AW circulation in the Canada Basin is sensitive to the strength of the surface stress forcing.

The AW that crossed the Lomonosov Ridge, returns toward Fram Strait along the North American continental shelf with 0.9 Sv recrossing the ridge near the shelf break. Finally, 2.4 Sv of now cooler and fresher AW exits the Arctic Ocean on the Greenland side of Fram Strait in the East Greenland Current. Apart from the Barents Sea, the Nares Strait in the Canadian Archipelago and Fram Strait, the Arctic Ocean is closed to AW flow since the Bering Strait and most of the Canadian Archipelago passages are too shallow to permit AW exchange. AW outflow occurs

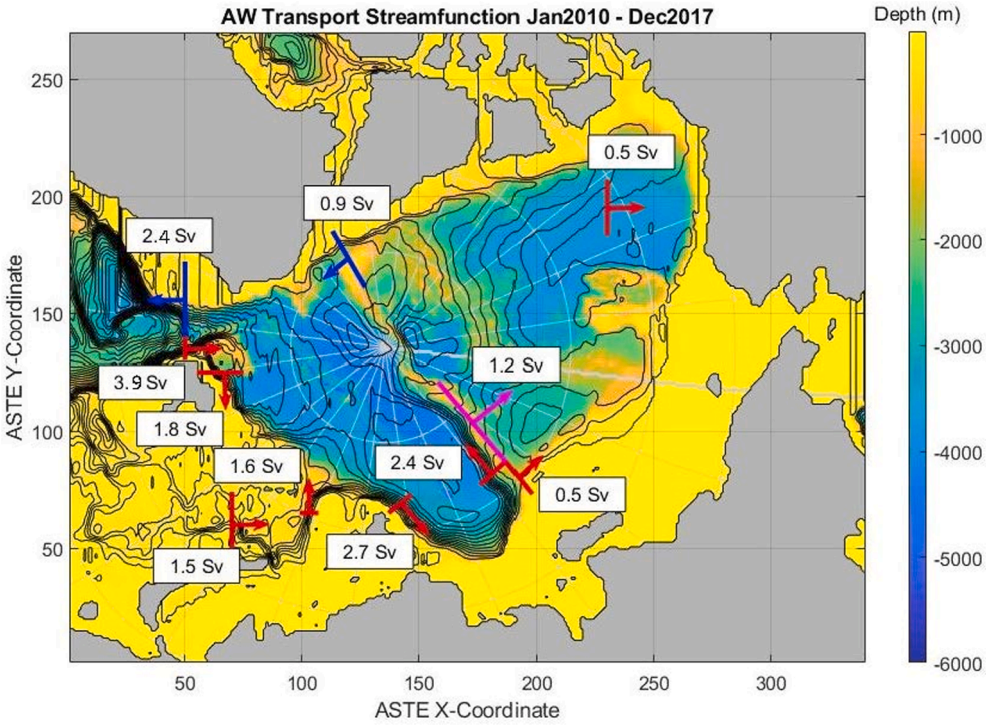

Fig. 8. Time-averaged volume transport streamfunction for the AW Layer in ASTE R1. Contour interval is 0.25 Sv. The time-averaged AW transport field is divergent due to water mass transformations within the Arctic Ocean and the AW volume in ASTE R1 increases with time over the averaging period. Both are responsible for the transport streamfunction being non-uniform along the North American coast.

mostly through Fram Strait and to a lesser extent through Nares Strait since the Barents Sea contributes only to AW inflow in the time average.

The (non-unique) depiction of the non-divergent, time-mean circulation of the AW Layer in ASTE R1 is similar to the full transport field, Fig. 9. The same locations used to compute the full volume transport yield estimates that are a few tenths of a Sverdrup less than the full streamfunction case, as could be expected since the full transport is the sum of the non-divergent and divergent fields. The non-divergent streamlines more clearly show the AW from Fram Strait following isobaths in the St. Anna Trough. The cyclonic circulation on the Eurasian side of the Amundsen Basin is better defined with additional closed streamlines. The same AW bifurcation occurs at the Lomonosov Ridge

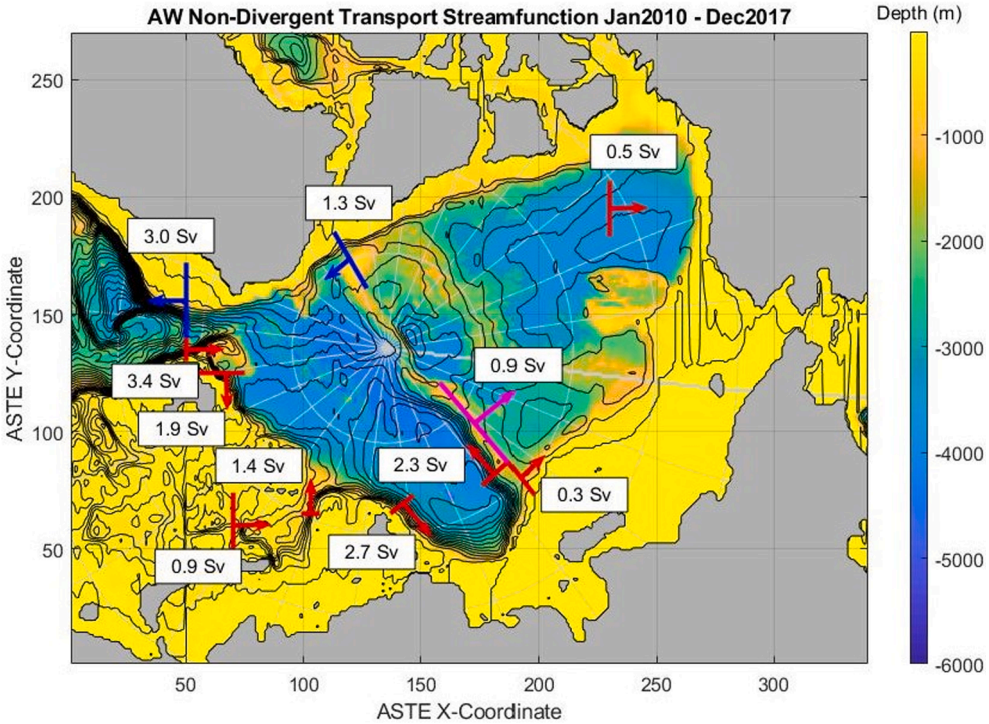

Fig. 9. Depiction of a non-unique representation of the non-divergent time-averaged AW transport streamfunction in the Arctic Ocean. Contour interval is 0.25 Sv.

with the majority of AW following the ridge rather than continuing as a Circumpolar Boundary Current. Along the ridge, AW spills over into the Makarov Basin rather than returning directly to Fram Strait, although the cross-ridge transport is 0.3 Sv less than that of the full flow. The anticyclonic circulation in the Beaufort Gyre remains. Since the non-divergent streamfunction is forced to zero at the North American coast, the return flow toward Fram Strait is stronger along the Canadian Archipelago with 1.3 Sv recrossing the Lomonosov Ridge. The outflow in Fram Strait also increases to 3.0 Sv.

Water mass transformation within the Arctic Ocean has been discussed as an important driver for AW flow into the Arctic Ocean (e.g. Timmermans and Marshall, 2020). As described in Section 2, the ASTE R1 time-averaged overturning and storage change was explored in a three-layer decomposition, Fig. 10. Both the Surface Layer and AW volumes swelled over the analysis period while the Deep and Bottom Water Layer shrank. Confidence bounds (95%) on these rates of volume change are based on uncertainty in linear volume trend estimates with time. As shown, the total volume of Arctic Ocean waters in this budget is conserved.

Over the 2010–2017 period, the Deep and Bottom Water Layer in ASTE R1 exhibits an overall rate of volume decrease with time of 1.5 Sv and a net outflow of 1.9 Sv through Fram Strait. The confidence bounds (95%) on the mean Fram Strait transport estimate (and the other mean inflow and outflow estimates) is based on the variance of the (respective) monthly transport estimates. Deep and Bottom Water is blocked from entering or exiting through Bering Strait and Canadian Archipelago due to the much shallower water depths in these passages. Thus, 0.4 Sv of AW must be transformed into Bottom Water on average to conserve volume. The uncertainty of the transformation rate estimate is based on propagation of error.

The volume of the AW Layer in ASTE R1 increased by an average rate of 1.4 Sv during the averaging period. The model has a mean net inflow of AW via the Barents Sea and Fram Strait of 3.1 Sv and a net outflow of 0.3 Sv through the Canadian Archipelago in the Nares Strait. The continental shelf prevents AW from passing through Bering Strait. Including the inferred conversion of AW to Deep and Bottom Water, volume conservation dictates a 1.0 Sv transformation of AW to Surface Water on average. A propagation of error calculation yields the 0.4 Sv uncertainty estimate (95%) for the transformation rate.

ASTE R1 has a mean net inflow of Surface Layer water at Bering Strait of 1.0 Sv which is consistent with direct transport observations (Woodgate, 2018), a net outflow via the Canadian Archipelago of 1.5 Sv (chiefly through Nares Strait), and a net outflow at Fram Strait/Barents Sea of 0.8 Sv. Over the analysis period, ASTE R1 has a net precipitation minus evaporation plus runoff of 0.1 Sv (roughly consistent with the Aagaard and Carmack, 1989 figure but half that of more recent analyses as reported by Carmack et al., 2016). ASTE R1 has a small (less than 0.1 Sv) average net export of sea ice water equivalent over the analysis period. The sum of these Surface Layer fluxes and volume rate of change (−0.3 Sv) is not statistically different from zero based on the 95% confidence bound obtained by propagation of error (0.4 Sv). It is known that ASTE conserves mass at each time step to a high degree of precision (Nguyen et al., 2021). Total volume conservation for the full Arctic domain using the monthly ASTE R1 velocity fields (co-located with the scalar data from the ASTE staggered grid), estimated P-E + RO and ice transport fields, but neglecting flow in shaved cells at the bottom and eddy fluxes, was verified to better than 0.1 Sv with the 2010–2017 average residual less than 0.05 Sv. However, error was incurred in developing the water mass transformation scheme when interpolating level model output to estimate transport in layers bounded by isopycnals, in addition to the lack of accounting in this analysis for flow within shaved grid cells and the neglect of eddy bolus. We nevertheless believe our ability to perfectly close the time-averaged overturning circulation budget based on the ASTE R1 monthly mean output is principally constrained by the statistical uncertainty of the mean horizontal volume transport estimates at each gateway.

Following the inverse model procedures detailed by Tsubouchi et al. (2018), Tsubouchi et al. (2019) provide monthly estimates of water properties and velocities across the major passages between the Arctic Ocean and subpolar seas for the period October 2004 to May 2010. For comparison with ASTE R1, monthly estimates of the inverse model transports in and out of the Arctic through Fram Strait, the Barents Sea

Table 1
Time-averaged volume transport estimates (Sv) with statistical uncertainties (in parentheses) based on inverse model results of Tsubouchi et al. (2019). For comparison, time-averaged ASTE R1 layer transports for the period 2010–2017 are also provided. Positive transports correspond to flow into the Arctic Ocean. "n.a." stands for "not applicable"

	Fram Strait	Barents Sea	Davis Strait	Bering Strait
Tsubouchi et al (2019)				
Surface Layer	−0.8 (0.1)	0.7 (0.1)	−1.6 (0.1)	1.0 (0.1)
AW	1.9 (0.2)	1.6 (0.2)	−0.2 (0.2)	0. (n.a.)
Deep-Bottom Layer	−2.5 (0.3)	−0.1 (<0.1)	0. (n.a.)	0. (n.a.)
ASTE R1 2010–2017				
Surface Layer	−1.0 (<0.1)	0.2 (<0.1)	−1.5 (0.1)	1.0 (0.1)
AW	1.5 (0.2)	1.6 (0.2)	−0.3 (0.1)	0. (n.a.)
Deep-Bottom Layer	−1.9 (0.2)	0. (n.a.)	0. (n.a.)	0. (n.a.)

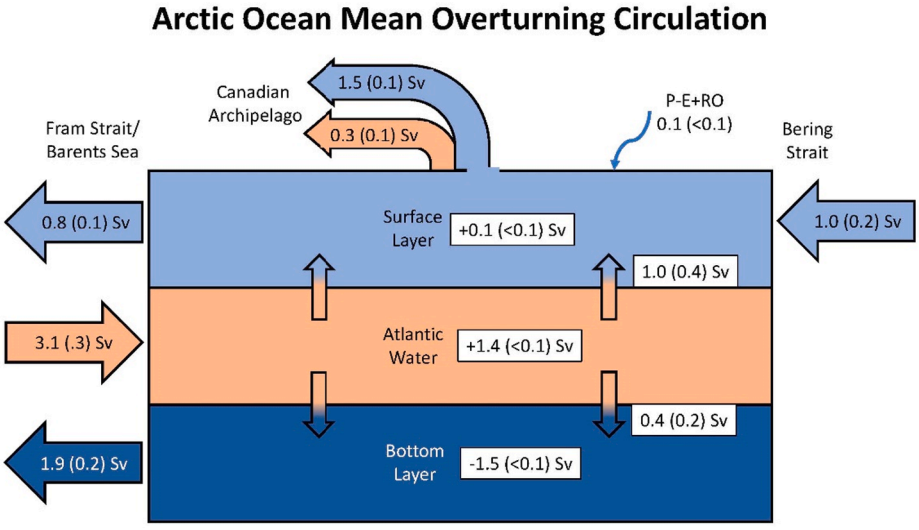

Fig. 10. The time-averaged overturning circulation in ASTE R1 for the period from January 2010 through December 2017. The analysis yielded estimates of the time-averaged net volume transports into and out of the Arctic (horizontal arrows) and time-average rates of volume changes (values shown in boxes within each layer) for three layers: a Surface Layer (waters with $\sigma_{0.2} < 28.2$ kg/m^3), the AW Layer, and a Deep and Bottom Water Layer ($\sigma_{0.2} >$ 28.9 kg/m^3). Fluxes between layers (displayed next to vertical arrows) are inferred from volume conservation. Average rates of volume transport and volume change are shown together with 95% confidence bounds (in parentheses). Results are rounded to the nearest 0.1 Sv.

opening, Davis Strait and Bering Strait were derived for the same three layers presented above, Table 1. Despite very different analysis procedures (box inverse model versus fully non-linear state estimate) and time period, the time-average transport estimates into and out of the Arctic Ocean in the three layers based on the Tsubouchi et al. (2019) data are remarkably similar – perhaps because both data products are constrained in part by the same observations (although treated very differently).

3.3. Seasonal variability

The mean annual cycle of AW flow into and out of the Arctic Ocean was constructed by averaging the volume transport estimates across model grid line x = 50 (see Fig. 1) for each month of the calendar year between 2010 and 2017, Fig. 10. The AW volume transports into and out of the Arctic are greatest during winter and least during summer. The AW inflow through Fram Strait is generally over twice as large as the Barents Sea inflow for all months, but as seen in the time-mean AW circulation, a significant fraction of the AW entering via Fram Strait recirculates back south rather than entering the Arctic Ocean proper north of Svalbard. Possibly manifesting inertial recirculation dynamics, the seasonal cycle in AW inflow in Fram Strait is nearly in phase with the AW outflow through that passage. However, the average seasonal range of the Fram Strait inflow (2.7 Sv difference between winter and summer) is greater than that of the Fram Strait outflow (1.1 Sv) as well as that of the Barents Sea net inflow (1.9 Sv). The seasonal range of the net AW inflow (3.2 Sv) is comparable to the annual mean.

The mean annual cycle of net AW inflow based on the monthly Tsubouchi et al. (2019) fields integrated over the AW isopycnal bounds used here is quite consistent with the ASTE R1 results shown in Fig. 10. For those inverse model results, net input is maximum in January at 5.0 Sv and reaches a minimum in June at 1.2 Sv. A secondary minimum of 1.7 Sv is achieved in August. Using an alternate definition for the AW layer, Tsubouchi et al. (2021) derive a mean annual cycle of net AW inflow that has opposite phase to that shown in Fig. 11. We note that the Tsubouchi et al. 2021 time-averaged AW inflow greatly exceeds that derived here from ASTE R1 – a consequence of the different AW definition.

The ASTE R1 mean seasonal variability in AW inflow extends throughout the boundary current systems. The average speed of the AW along the Lomonosov Boundary Current contour, Fig. 1, is fastest in January with an average speed of slightly greater than 2.6 cm/s. The slowest AW Layer flow occurs in July with an average speed of approximately 1.9 cm/s. The transition from faster winter speeds to slower summer speeds occurs over a shorter amount of time with a longer summer relaxed state extending into late summer/early fall (not shown).

3.4. Interannual variability

The monthly time series of AW transports through Fram Strait and the Barents Sea, Fig. 12, clearly manifests the seasonal cycle just discussed with maximum inflows in winter and minima in summer. These seasonal variations are superimposed on an overall increase in volume transport that occurs in 2004 to 2005 at all three branches. This is most clearly seen in the wintertime maximum values. The Fram Strait AW inflow winter maximum in 2002 is less than 3 Sv but increases to 5 Sv in 2004, reaching its highest value of approximately 8 Sv in January 2005. In all later years, the maximum remains between 5 and 7 Sv, all greater than the maximums before January 2004. The AW exiting through Fram Strait also increases its throughput after January 2003 with a maximum in January 2005 of −3.6 Sv. Starting in 2005, winter maximums are approximately −3 Sv: greater than the maximums prior to January 2005 which are less than −2 Sv. The increase in Barents Sea AW inflow occurs between 2004 and 2006. Unlike the Fram Strait transports, the maximum volume transport, 3.9 Sv, occurs in January 2006 rather than 2005. Also, the seasonal minimum values for the Barents Sea inflow do not show an overall increase after 2004, ranging between 0.5 and 1.0 Sv during the entire period. From a longer time series beginning in 1993, Tsubouchi et al. (2021) report an increase in temperature transport into the Arctic starting somewhat earlier than the surge in ASTE R1 (between 2001 and 2002).

The AW Layer velocity along the Lomonosov Boundary Current contour for each month of ASTE R1 output documents a striking change in model circulation during the analysis period, Fig. 13. For the first ~2 years of the state estimate, the along-contour circulation is dominantly

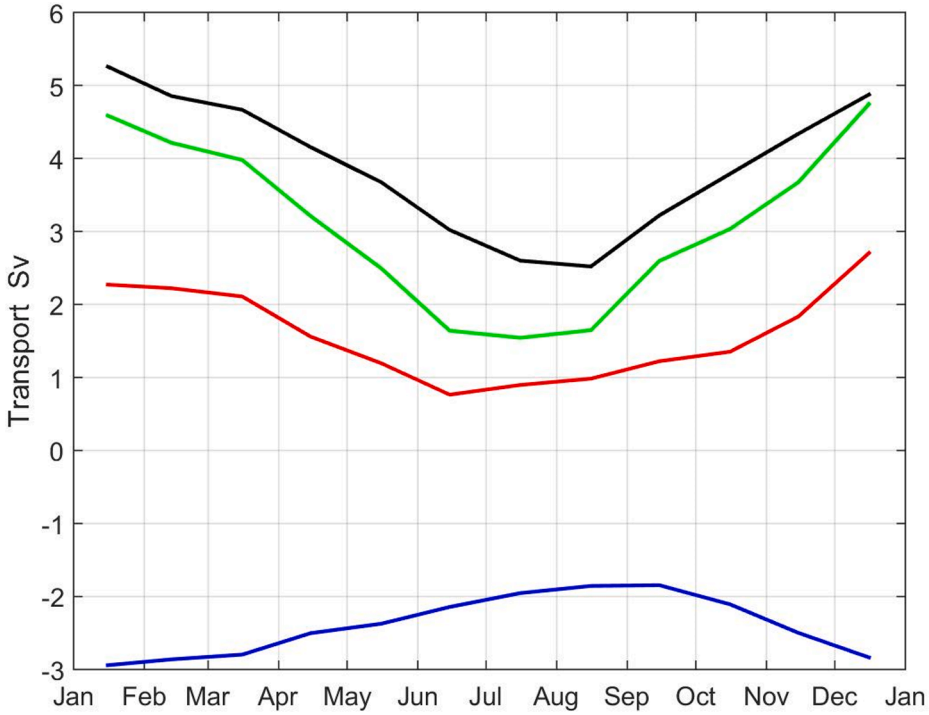

Fig. 11. The average seasonal cycle of AW volume transport inflow (black line) and outflow (blue line) through Fram Strait and AW inflow through the Barents Sea (red line) for the period January 2010 through December 2017. Positive values indicate flow into the Arctic Ocean. The mean net AW inflow each month is shown in green. Transport estimates were made across the model grid line X = 50 (see Fig. 1). (For interpretation of the references to color in this figure legend, the reader is referred to the web version of this article.)

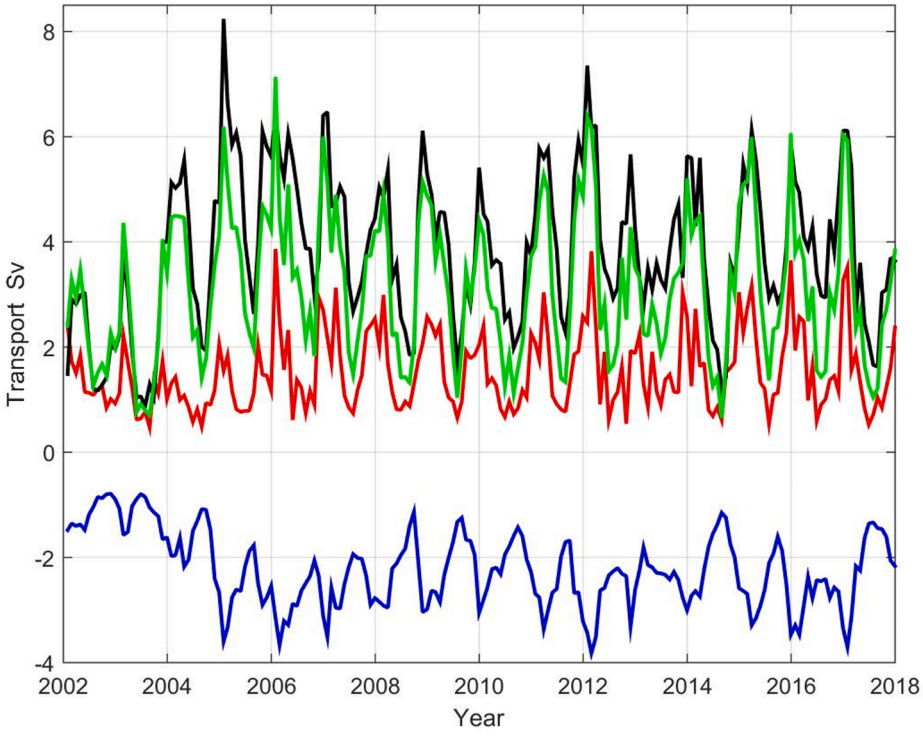

Fig. 12. Time series of the AW volume transport inflow (black line) and outflow (blue line) through Fram Strait and AW inflow through the Barents Sea (red line) for the full period of ASTE R1 output. Positive values indicate flow into the Arctic Ocean. The net AW inflow each month is shown in green. Transport estimates were made across the model grid line X = 50 (see Fig. 1). (For interpretation of the references to color in this figure legend, the reader is referred to the web version of this article.)

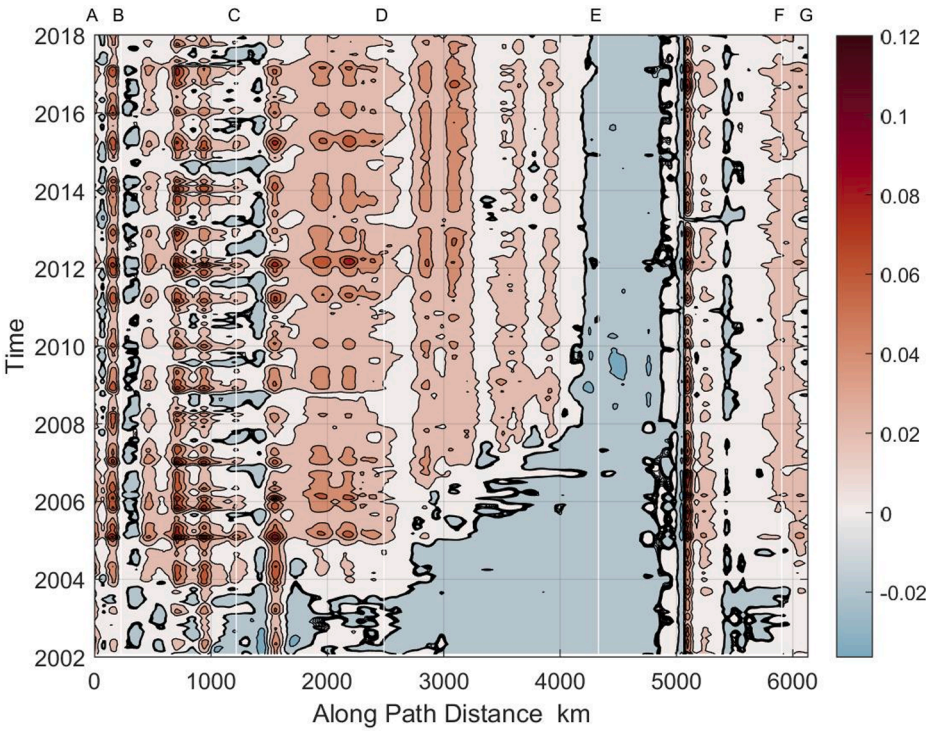

Fig. 13. Hovmöller diagram of the AW-Layer velocity component (units of m/s) parallel to the Lomonosov Boundary Current contour shown in Fig. 1. Positive values are directed cyclonically around the Arctic Ocean. Key geographic locations along the path marked in Fig. 1 with letter codes are annotated here with white lines and corresponding letter codes. The zero isotach is marked with bold line. Path angle and AW-Layer velocity heading were low-pass filtered over ~50 km prior to contouring.

anticyclonic. But beginning in 2004, the flow along the Lomonosov Ridge begins to reverse direction, as indicated by the zero isotach moving to greater along-path distance with time between path locations D and E. By 2006, the boundary current flow enters an approximate steady state that extends to the end of the ASTE R1 simulation. Prior to the reversal, the Lomonosov Boundary Current along-path velocity is weakly negative (anticyclonic); afterwards, the average current velocity along the path is cyclonic at ~0.15 m/s, ranging seasonally between ~0.1 and 0.3 m/s. The zero isotach contour propagates along the Lomonosov Ridge towards North America at a similar speed of ~0.14 m/s, suggesting the flow reversal is advective in character, as opposed to a topographic wave disturbance that travels much faster. Negative along-contour velocity persists throughout the state estimate period at path distances between ~4200 and 5000 km (between the Pole and Greenland): location of the anticyclonic gyre noted in the time-averaged streamfunction map in Fig. 8.

The change in ASTE R1 AW circulation pattern is visualized in streamline maps at four-year interval beginning with January 2002, Fig. 14. At that time, the strongest model AW currents are near the AW inflow areas and along the continental shelf of the Canadian Archipelago. Outside of these areas, the AW flow is generally 0.2 m/s or less. From the AW entrance regions (Fram Strait and the St. Anna Trough), the AW flows across the Nansen and Amundsen Basin toward the Lomonosov Ridge. On the Amundsen Basin side of the Lomonosov Ridge, the model AW flow is directed toward Eurasia. This is opposite the time-mean AW circulation described in Section 3.2 based on the 2010–2017 time-mean AW flow. The AW that crossed the Lomonosov Ridge at the Eurasian continental shelf flows into the mid Makarov Basin and along the Eurasian continental shelf. The Mendeleyev Ridge turns the AW toward the mid Makarov Basin with most of the AW eventually joining a cyclonic circulation in the Beaufort Gyre. The AW forms a stronger current along the North American continental slope as a return flow toward Fram Strait.

The AW flow in January 2006 exhibits several differences compared to January 2002 and more closely resembles the later time-mean circulation. Some of the AW entering Fram Strait turns to the east north of Svalbard and follows the continental slope rather than continuing into the mid basin. The Fram Strait and Barents Sea AW meet in the St. Anna Trough to form a strong current with a speed of approximately 0.1 m/s. AW follows a cyclonic path into the Laptev Sea with a bifurcation of AW flow at the Lomonosov Ridge. Some of the AW turns poleward at the Lomonosov Ridge, follows the ridge and crosses into the Makarov Basin. There is not a clear path of AW which parallels the Lomonosov Ridge and directly returns to Fram Strait. Instead, the AW spills over the ridge and flows toward the Canadian Archipelago in the Makarov Basin. A portion of AW also crosses the Mendeleyev Ridge into the Canada Basin. The AW that does not turn at the Lomonosov Ridge continues as the Arctic Circumpolar Boundary Current along the Eurasian continental shelf. The anticyclonic AW flow in the Beaufort Gyre is beginning to take shape but there remains some cyclonic flow east of the Gyre center. All the mid subbasins contain recirculations adjacent to the main AW flow paths. The return flow of AW toward Fram Strait on the North American side of the Arctic Ocean remains relatively strong.

In January 2010, the AW flow field indicates a much stronger flow along the Lomonosov Ridge with fewer streamlines crossing the ridge. Also, there are streamlines showing that some AW follows along the ridge and returns to Fram Strait which is the generalized flow path described by Rudels et al. (2012) and Mauritzen et al. (2013). The Arctic Circumpolar Boundary Current is weaker with no clear signature from the Mendeleyev Ridge to the continental shelf near Alaska. The streamlines provide better definition of the anticyclonic AW circulation in the Beaufort Gyre while flow remains less than 0.1 m/s in most locations. This depiction of the AW flow resembles the time-mean circulation from 2010 through 2017 discussed in Section 3.2. The AW flow in January 2014 is consistent with the pathways in January 2010. The meandering positions of the mid basin recirculations are discernible. The AW current speed is lower in most locations compared to January 2010 and January 2006.

These ASTE R1 results indicate that a surge of AW entered the Arctic Ocean via Fram Strait and the Barents Sea in 2004. The augmented AW flow spreads into the Arctic Ocean along boundary, increasing the speed of the boundary current as the surge moves into the Laptev Sea and later along the Lomonosov Ridge, resulting in a reversal of the latter flow. A new quasi-steady-state for the AW Layer where the direction and speed of AW is consistent in time and with previous investigations begins by 2010. While a surge of AW into the Arctic early in this century has been reported previously, reversal of the flow along the Lomonosov Ridge seen in ASTE R1 is uncorroborated due to lack of direct observations.

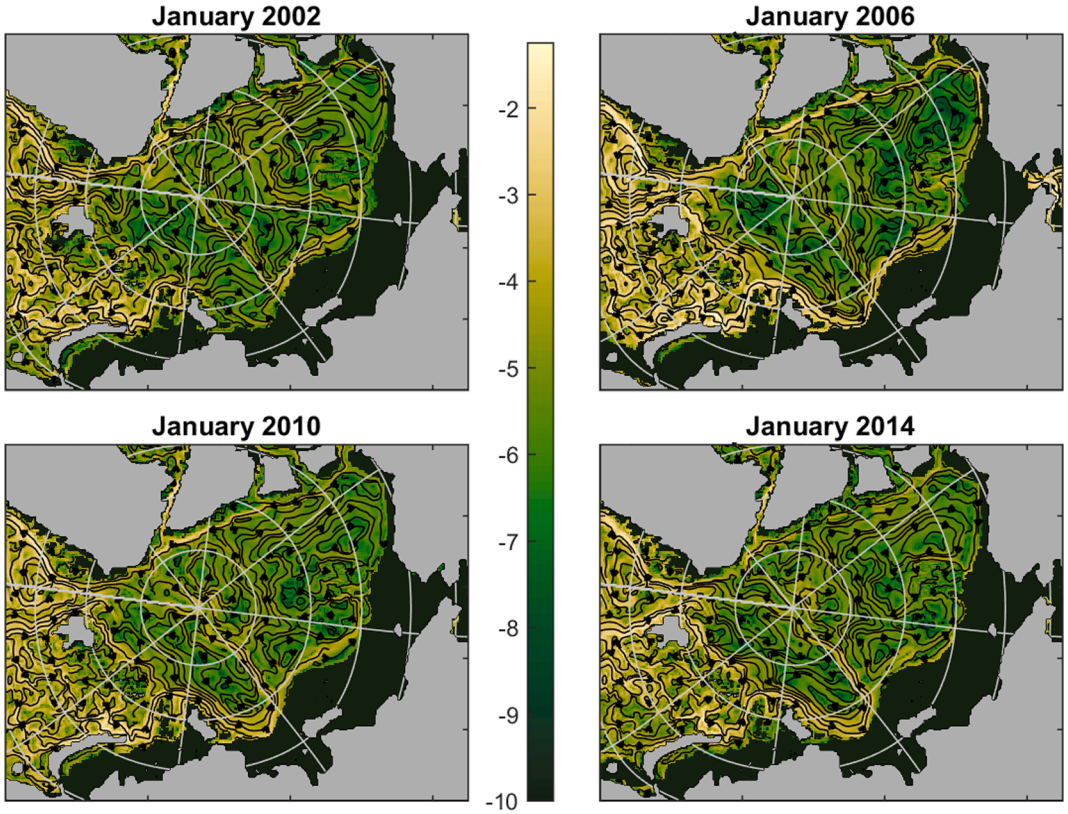

Fig. 14. Streamlines of ASTE R1 AW Layer velocity at 4-year intervals - top left: January 2002, top right: January 2006, bottom left: January 2010, bottom right: January 2014. The colors indicate the speed of the flow with direction indicated by arrows on the streamline contours. For visual enhancement, the natural log of the speed in m/s is displayed (with colorbar in the middle). Black areas are where no water existed between the AW bounding isopycnals. Latitude circles are drawn at 5° interval and meridians at 45° interval. (For interpretation of the references to color in this figure legend, the reader is referred to the web version of this article.)

The current direction early in the analysis period is not consistent with prior inferred circulation diagrams. The data base underpinning the early years of the ASTE R1 state estimate may not be sufficient to accurately define the initial flow direction.

As discussed in Section 2, the AW Layer temperature generally increases over the duration of ASTE R1 output; the increase in temperature commences with the surge of AW discussed above. In January 2002, the warmest AW is near Fram Strait with layer temperatures exceeding 1.5 °C along the continental shelf north of Svalbard and Franz Josef Land, Fig. 15. In 2006, AW temperatures greater than 1.5 °C advanced cyclonically into the Arctic Ocean reaching the St. Anna Trough and the continental shelf near the Laptev Sea. AW Layer temperatures greater than 1.5 °C then extended along the Lomonosov Ridge, crossing into the Makarov Basin on the Eurasian side of the Arctic Ocean and up to the pole by January 2010. The surge of warm AW surrounds cooler water, with temperatures near 1 °C, in the Amundsen Basin away from the Lomonosov Ridge and the continental shelf. By January 2014, this cooler water has warmed to around 1.5 °C as the heat is spread to the mid basin and the magnitude of the temperature gradient between the shelf/ridge and the mid basin water has decreased. The warm AW water near 1.5 °C has also advanced to the Canadian Archipelago and mid Makarov Basin by this time. Parallel evolutions of the depth of the lower AW bounding isopycnal surface and AW Layer thickness are also observed (Grabon, 2020). A similar pattern of boundary current warming is presented by Polyakov et al. (2011); ASTE R1 sheds light on how this signal may spread into the ocean interior.

4. Discussion and conclusions

This study is the first to analyze the ASTE Release 1 monthly mean output to characterize the AW Layer in the Arctic Ocean and compare the state estimate output to observed AW Layer properties. While monthly mean output does not permit an analysis of AW property variability due to eddies, it does support analyses of basin wide seasonal to interannual AW variability and a description of the AW time-mean circulation and its properties.

The ASTE R1 solution analyzed here was obtained after 62 iterations of optimization. A significant, sustained shift in AW properties is observed in the state estimate 2–4 years after the solution initial time of January 2002. (Note that the state estimate fields examined here were obtained after an extended model spin up period, and the initial conditions of the run were part of the ASTE control space, Nguyen et al., 2021.) Generally consistent with the observational analysis of Polyakov et al. (2011), a surge of AW is observed in ASTE R1 to enter the Arctic Ocean in 2004 at Fram Strait, leading to increases the AW Layer mean potential temperature, bottom AW bounding isopycnal depth, and boundary current speed as it traverses the Arctic Ocean. Since there is not much change in the top AW bounding isopycnal, the AW Layer thickness throughout the Arctic Ocean also increases. The surge enters the Arctic Ocean proper along the continental shelf north of Svalbard and traverses cyclonically to the Laptev Sea with a bifurcation in the flow at the Lomonosov Ridge. The signal moves along the major AW boundary currents and ridge at less than 0.2 m/s which indicates this signal is likely advected in the Arctic Ocean. As the surge extends along the Lomonosov Ridge from 2004 through 2008, the direction of the flow there reverses, from towards Eurasia to towards North America. Some of the surge crosses the Lomonosov Ridge as AW property changes are seen to spread into the Makarov Basin and eventually extend to the other side of the Mendeleyev Ridge into the Canada Basin while enroute to the North American continental shelf. Affected AW properties change first along the AW boundary currents and later spread into the mid basins. The magnitude of the change for each affected AW parameter is dependent upon location and distance from AW inflow areas, with the largest changes near AW source regions. The net effect of the post-surge circulation is a warmer, thicker AW layer, possibly interpretable as increased “Atlantification.”

The cause of the surge in ASTE R1 has been hypothesized to be connected to changes in the ocean state and circulation much further

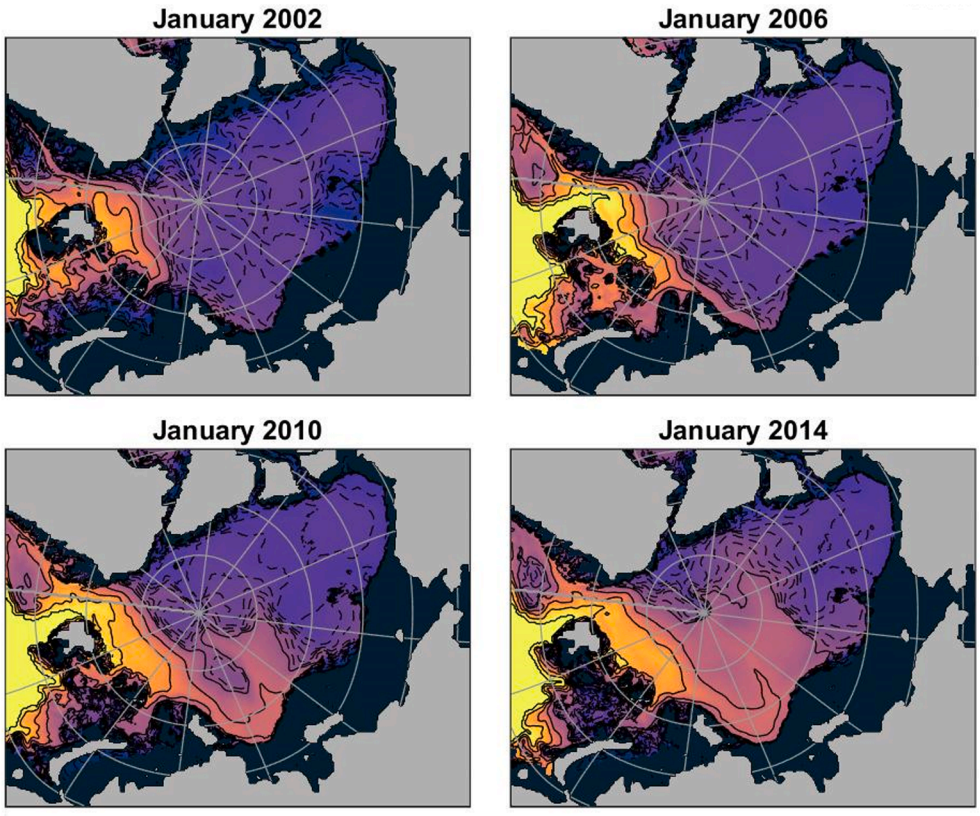

Fig. 15. Distribution of ASTE R1 AW Layer potential temperature at 4-year intervals - top left: January 2002, top right: January 2006, bottom left: January 2010, bottom right: January 2014. Temperatures in each panel range between −0.5 and 3.0 °C with solid contours at 0.5 °C increment drawn between 1 and 3 °C and dashed contours at 0.1 °C increment between −0.5 and 1.0 °C. Black areas are where no water existed between the AW bounding isopycnals. Latitude circles are drawn at 5° interval and meridians at 30° interval.

upstream in the North Atlantic and Nordic Seas (Nguyen et al., 2021). The change resulted in a shift of the partitioning of AW inflow between the Iceland-Faroe and Faroe-Scotland Ridges and stronger northward transport of AW into the Arctic Ocean across Fram Strait. The surge adjusts the model to a quasi-steady AW circulation for the rest of the state estimate period that aligns with accepted AW circulation schemes. The described behavior raises the question if a wave, such as a Kelvin wave, is propagating along bathymetry and adjusting the model to a new steady-state. A wave seems unlikely since the speed of the surge along the Arctic Ocean boundary was of the same magnitude as the boundary current speed, much slower than the theoretical first vertical mode wave speed. Moreover, the time stepping employed in ASTE quickly damps fast Kelvin waves in a few wave periods (Nguyen et al., 2020).

Two physical mechanisms driving the AW circulation into and out of the Arctic Ocean have been developed in previous research. One evokes a two-layer, estuary framework as described by Rudels (1989) and Stigebrandt (1981), where a cool, fresh layer overlies a warm, salty layer. For a fixed freshwater input at the surface (e.g. river-runoff and net precipitation), the amount of AW entering the Arctic Ocean depends on the mixing between the two layers, with increased mixing resulting in more AW entering the Arctic Ocean. The internal framework of ASTE could be used to test if the surge is a result of an increase in the overturning circulation since the surge does not occur until a couple years after the initial time of the state estimate.

The other concept for driving AW flow into and around the Arctic Ocean is based on wind forcing and potential vorticity (PV) dynamics. In the absence of forcing, PV is conserved, leading to the requirement that flow is along f/H contours where f is the Coriolis parameter and H is the water depth. Since the f-plane approximation (constant f) can be applied to the Arctic, PV contours closely follow isobaths. As discussed in Timmermans and Marshall (2020), the integral of the wind stress curl within an enclosed f/H contour may be related to the circulation around that contour and could result in an AW Layer that is driven by the wind stresses in the Nordic Sea. Forcing external to the Arctic Ocean could thus be responsible for the surge observed within ASTE R1. Since the ASTE domain extends to 32.5°S, surface forcing in the Nordic Sea could be tested within the model as a potential source of increased AW flow.

A quasi-steady-state circulation is attained in ASTE R1 by 2010 that continues through the end of the state estimate period. The mean AW inflow at Fram Strait (~3.9 Sv, with ~2.1 Sv immediately recirculating) is greater than the Barents Sea inflow (~1.6 Sv); the mean net Fram Strait inflow is comparable to that in the Barents Sea. The mean AW outflow through Fram Strait (~2.4 Sv) is greater than that through the Canadian Archipelago (~0.3 Sv), which is largely limited in ASTE R1 to the Nares Strait. The ocean interior time-mean circulation during this time period contains two boundary currents; the Lomonosov Boundary Current and the Circumpolar Boundary Current with the majority of the recently-entered AW turning poleward at the Lomonosov Ridge (~2.4 Sv vs. ~0.5 Sv). Much of the northward AW flow is seen to leak over the Ridge into the basins beyond. That a significant fraction of the AW crosses the Lomonosov Ridge rather than paralleling the ridge and turning directly toward Fram Strait is not consistent with the subjective AW flow schematics such as presented in Mauritzen et al. (2013) and Rudels et al. (2012). Additional smaller, semi-permanent AW recirculations were seen adjacent to the Lomonosov Ridge and primary boundary currents as well as under the Beaufort Gyre.

The amount of AW crossing the Lomonosov Ridge into the Makarov Basin in ASTE R1, either at the ridge-continental slope junction or farther north along the ridge, could be sensitive to the model resolution. It is well known that coarse grid resolution or the representation of the bathymetry in numerical models can limit the flow of water over bathymetric obstructions. Mooring observations, preferentially about the deep passages along the Lomonosov Ridge, could provide key estimates of the AW volume transport and associated heat flux into the basins beyond. Additional observations could be obtained by UUVs operating along the ridge. Of course, operating in this region is difficult due to sea ice and seasonal conditions that constrain access to this area. However, the additional data would assist in constraining ocean state estimates such as ASTE and provide better estimates for the AW circulation in this region, with implications for improving estimation of the overall global energy budget due to the water mass transformations occurring within the Arctic Ocean.

The ASTE R1 mean seasonal cycle of AW in the Arctic Ocean has the greatest (least) inflow of AW and most (least) vigorous boundary currents during winter (summer). Interestingly, the seasonal winter enhancement of AW inflow via Fram Strait and the Barients Sea is in phase with the seasonal maximum in Fram Strait outflow. This result could be further examined to see if a wind-driven model for AW circulation reproduces similar seasonal fluctuations in volume transport. Modification to a simplified three-layer model such as the one presented by Spall (2013) developed with a uniform-stress over the Arctic Ocean and Nordic Seas, could further analyze mechanisms causing variations in AW volume transport circulation.

The divergent part of the ASTE R1 time-averaged flow characterizes the overturning circulation and thus water mass transformations within the Arctic Ocean. Analysis of the Surface Layer revealed only a 0.1 Sv rate of volume increase from 2010 to 2017 while the AW Layer had an average rate of volume increase of 1.4 Sv and the Bottom Layer a volume decrease rate of 1.5 Sv. This is reflected in the deepening with time of the lower AW bounding isopycnal documented in this analysis. When combined with net ocean transport estimates, continuity reveals that in ASTE R1, more AW is converted to relatively fresh, cold Surface Layer water (1.0 Sv) than to more saline and colder Deep and Bottom Layer water (0.4 Sv). Pemberton et al. (2015, and references cited therein) examine this “double estuary” model for the Arctic by applying the Hieronymus et al. (2014) watermass transformation framework to numerical model output. Forryan et al. (2019) utilize an endpoint mixing model formalism in combination with the Tsubouchi et al. (2012) transport scheme to quantify the upper limb of the overturning circulation. The sense of these reported water mass conversions are in the same directions as inferred from this analysis of ASTE R1. Specific rates differ but are in large measure within the stated uncertainties.

The mechanisms driving these watermass conversions were not investigated here but could be conducted within the ASTE framework (Abernathey et al., 2016). Specific locations to investigate include mixing along the continental shelf and ridges which are likely locations where AW is transformed to Bottom Layer water. The thickening of the AW Layer and thinning of the Bottom Layer might indicate that ASTE R1 is not transforming enough AW to denser waters. This may be a result of limited deep hydrographic data to constrain the state estimate. Additionally, a spatial analysis of where AW is preferentially converted to Surface Layer water would provide insight into the processes driving this transformation, the associated vertical heat flux and its impact on the overlying sea ice.

The ASTE framework provides the opportunity to investigate parameters determining AW properties in the Arctic Ocean. The mean AW Layer temperature is warmest in Fram Strait when it enters the Arctic Ocean via the West Spitsbergen Current. The warmest water follows the boundary currents with cooler AW water away from the shelves and ridges. The thickest AW Layer is along the continental shelf from Franz Josef Land to the Laptev Sea and along the Lomonosov Ridge up to the pole. The ASTE R1 is constrained by observations to provide a best-estimate of Arctic Ocean properties, but in the AW Layer, the difference between the state estimate and observations generally increases during the optimized period, with the AW Layer in ASTE R1 being generally warmer and thicker than observations. More investigation into what parameters are causing the best-estimate to deviate from observations over time, including a more complete observational comparison than conducted in this study, would reveal determining factors for AW Layer evolution in the model.

CRediT authorship contribution statement

Jeffrey S. Grabon: Conceptualization, Methodology, Writing – original draft. **John M. Toole:** Conceptualization, Methodology, Writing – original draft, Supervision, Funding acquisition. **An T. Nguyen:** Methodology, Software, Writing – original draft, Funding acquisition. **Richard A. Krishfield:** Data curation, Validation, Writing – original draft.

Declaration of Competing Interest

The authors declare that they have no known competing financial interests or personal relationships that could have appeared to influence the work reported in this paper.

Acknowledgements

This work is based on the dissertation of the lead author submitted in partial requirement of a M.S. degree from the Massachusetts Institute of Technology/Woods Hole Oceanographic Institution Joint Program in Oceanography. The lead author's participation was funded by the United States Navy's Civilian Institution (CIVINS) Program. The contributions to this study by the junior authors were supported by the National Science Foundation (JMT and RAK grant PLR-1603660; ATN grant NSF-OPP-1603903). Isabela Le Bras kindly calculated the layer transport estimates in Table 1 that were derived from the fields provided by Tsubouchi et al. (2019). The authors thank S. Bacon and an anonymous reviewer for constructive advice for improving our presentation.

Data availability

The full ASTE R1 solution is publicly available through the UT-Austin ECCO portal at: https://web.corral.tacc.utexas.edu/OceanProjects/ASTE/, provided by the Texas Advanced Computing Center (TACC). The monthly mean fields are additionally stored in a compressed format on Amazon Web Services (AWS) servers, provided by TACC at https://s3.console.aws.amazon.com/s3/buckets/aste-release1/?region=us-east-2. See Nguyen et al. (2021) for details. The hydrographic observations examined in this study were accessed from the National Centers for Environmental Information (https://www.ncei.noaa.gov/) and the NSF Arctic Data Center (https://arcticdata.io/).

References

Aagaard, K., Carmack, E.C., 1989. The role of sea ice and other fresh water in the Arctic circulation. J. Geophys. Res. 94 (C10), 14485. https://doi.org/10.1029/JC094iC10p14485.

Abernathey, R., Cerovecki, I., Holland, P.R., Newsom, E., Mazloff, M., Talley, L.D., 2016. Water-mass transformation by sea ice in the upper branch of the Southern Ocean overturning. Nature Geosci. 9, 596–601. https://doi.org/10.1038/ngeo2749.

Aksenov, Y., Bacon, S., Coward, A.C., Nurser, A.J.G., 2010. The North Atlantic inflow to the Arctic Ocean: High-resolution model study. J. Marine Syst. 79 (1-2), 1–22. https://doi.org/10.1016/j.jmarsys.2009.05.003.

Aksenov, Y., Ivanov, V.V., Nurser, A.J.G., Bacon, S., Polyakov, I.V., Coward, A.C., Naveira-Garabato, A.C., Beszczynska-Moeller, A., 2011. The Arctic circumpolar boundary current. J. Geophys. Res. 116, C09017. https://doi.org/10.1029/2010JC006637.

Anderson, L.G., Jones, E.P., Koltermann, K.P., Schlosser, P., Swift, J.H., Wallace, D.W.R., 1989. The first oceanographic section across the Nansen Basin in the Arctic Ocean. Deep Sea Res. Part A Oceanogr. Res. Paper 36 (3), 475–482.

Andersson, M., Orvik, K.A., LaCasce, J.H., Koszalka, I., Mauritzen, C., 2011. Variability of the Norwegian Atlantic Current and associated eddy field from surface drifters. J. Geophys. Res. 116, C08032. https://doi.org/10.1029/2011JC007078.

Asbjørnsen, H., Årthun, M., Skagseth, Ø., Eldevik, T., 2020. Mechanisms underlying recent Arctic Atlantification. Geophys. Res. Lett., 47, e2020GL088036. https://doi.org/10.1029/2020GL088036.

Barton, B.I., Lenn, Y.-D., Lique, C., 2018. Observed Atlantification of the Barents Sea causes the Polar Front to limit the expansion of winter sea ice. J. Phys. Oceanogr. 48, 1849–1866. https://doi.org/10.1175/JPO-D-18-0003.1.

Beszczynska-Möller, A., Fahrbach, E., Schauer, U., Hansen, E., 2012. Variability in Atlantic Water temperature and transport at the entrance to the Arctic Ocean, 1997–2010. ICES J. Mar. Sci. 69 (5), 852–863.

Carmack, E.C., Yamamoto-Kawai, M., Haine, T.W.N., Bacon, S., Bluhm, B.A., Lique, C., Melling, H., Polyakov, I.V., Straneo, F., Timmermans, M.-L., Williams, W.J., 2016. Freshwater and its role in the Arctic Marine System: Sources, disposition, storage, export, and physical and biogeochemical consequences in the Arctic and global oceans. J. Geophys. Res. Biogeosci. 121 (3), 675–717. https://doi.org/10.1002/jgrg.v121.310.1002/2015JG003140.

Coachman, L.K., Barnes, C.A., 1961. The contribution of Bering Sea Water to the Arctic Ocean. Arctic, 14(3), Jan 1961.

Dmitrenko, I.A., Polyakov, I.V., Kirillov, S.A., Timokhov, L.A., Frolov, I.E., Sokolov, V.T., Simmons, H.L., Ivanov, V.V., Walsh, D., 2008. Toward a warmer Arctic Ocean: Spreading of the early 21st century Atlantic Water warm anomaly along the Eurasian Basin margins. J. Geophys. Res. 113 (C5) https://doi.org/10.1029/2007JC004158.

Fukumori, I., Fenty, I., Forget, G., Heimbach, P., King, C., Nguyen, A., Piecuch, C., Ponte, R., Quinn, K., Vinogradova, N., Wang, O., 2018. Data sets used in ECCO Version 4 Release 3. Retrieved from http://hdl.handle.net/1721.1/120472.

Forget, G., Campin, J.-M., Heimbach, P., Hill, C.N., Ponte, R.M., Wunsch, C., 2015. ECCO version 4: an integrated framework for non-linear inverse modeling and global ocean state estimation. Geosci. Model Dev. 8 (10), 3071–3104.

Forryan, A., Bacon, S., Tsubouchi, T., Torres-Valdés, S., Naveira Garabato, A.C., 2019. Arctic freshwater fluxes: sources, tracer budgets and inconsistencies. The Cryosphere 13, 2111–2131. https://doi.org/10.5194/tc-13-2111-2019.

Grabon, J.S., 2020. An analysis of Atlantic Water in the Arctic Ocean using the Arctic Subpolar gyre sTate Estimate and observations (Master's thesis). Massachusetts Institute of Technology/Woods Hole Oceanographic Institution Joint Program, Cambridge, Massachusetts, 90 pp. https://dspace.mit.edu/handle/1721.1/129018.

Hattermann, T., Isachsen, P.E., Appen, W.-J., Albretsen, J., Sundfjord, A., 2016. Eddy-driven recirculation of Atlantic Water in Fram Strait. Geophys. Res. Lett. 43 (7), 3406–3414.

Heimbach, P., Menemenlis, D., Losch, M., Campin, J.-M., Hill, C., 2010. On the formulation of sea-ice models. Part 2: Lessons from multi-year adjoint sea-ice export sensitivities through the Canadian Arctic Archipelago. Ocean Model. 33 (1-2), 145–158.

Hieronymus, M., Nilsson, J., Nycander, J., 2014. Water mass transformation in salinity–temperature space. J. Phys. Oceanogr. 44, 2547–2568. https://doi.org/10.1175/JPO-D-13-0257.1.

Jakobsson, M., Mayer, L., Coakley, B., Dowdeswell, J.A., Forbes, S., Fridman, B., Hodnesdal, H., Noormets, R., Pedersen, R., Rebesco, M., et al., 2012. The International Bathymetric Chart of the Arctic Ocean (IBCAO) Version 3.0. Geophys. Res. Lett. 39 (12).

Holloway, G., Dupont, F., Golubeva, E., Häkkinen, S., Hunke, E., Jin, M., Karcher, M., Kauker, F., Maltrud, M., Morales Maqueda, M.A., Maslowski, W., Platov, G., Stark, D., Steele, M., Suzuki, T., Wang, J., Zhang, J., 2007. Water properties and circulation in Arctic Ocean models. J. Geophys. Res. 112, C04S03. https://doi.org/10.1029/2006JC003642.

Jakobsson, M., Mayer, L., Coakley, B., Dowdeswell, J.A., Forbes, S., Fridman, B., Hodnesdal, H., Noormets, R., Pedersen, R., Rebesco, M., et al., 2012. The International Bathymetric Chart of the Arctic Ocean (IBCAO) Version 3.0. Geophys. Res. Lett. 39 (12).

Karcher, M., Kauker, F., Gerdes, R., Hunke, E., Zhang, J., 2007b. On the dynamics of Atlantic Water circulation in the Arctic Ocean. J. Geophys. Res. 112, C04S02. https://doi.org/10.1029/2006JC003630.

Kobayashi, S., Ota, Y., Harada, Y., Ebita, A., Moriya, M., Onoda, H., Takahashi, K., 2015. The JRA-55 reanalysis: general specifications and basic characteristics. J. Meteorol. Soc. Jpn 93 (1), 5–48.

Krishfield, R., Toole, J., Proshutinsky, A., Timmermans, M.-L., 2008. Automated Ice-Tethered Profilers for seawater observations under pack ice in all seasons. J. Atmos. Oceanic Technol. 25 (11), 2091–2105.

Lammers, R.B., Shiklomanov, A.I., Vörösmarty, C.J., Fekete, B.M., Peterson, B.J., 2001. Assessment of contemporary Arctic river runoff based on observational discharge records. J. Geophys. Res.: Atmos. 106 (D4), 3321–3334.

Lenn, Y.D., Wiles, P.J., Torres-Valdes, S., Abrahamsen, E.P., Rippeth, T.P., Simpson, J.H., Bacon, S., Laxon, S.W., Polyakov, I., Ivanov, V., Kirillov, S., 2009. Vertical mixing at intermediate depths in the Arctic boundary current. Geophys. Res. Lett. 36, L05601. https://doi.org/10.1029/2008GL036792.

Lind, S., Ingvaldsen, R.B., Furevik, T., 2016. Arctic layer salinity controls heat loss from deep Atlantic layer in seasonally ice-covered areas of the Barents Sea. Geophys. Res. Lett. 43 (10), 5233–5242.

Losch, M., Menemenlis, D., Campin, J.-M., Heimbach, P., Hill, C., 2010. On the formulation of sea-ice models. Part 1: Effects of different solver implementations and parameterizations. Ocean Model. 33 (1-2), 129–144.

Marshall, J., Adcroft, A., Hill, C., Perelman, L., Heisey, C., 1997. A finite- volume, incompressible Navier Stokes model for studies of the ocean on parallel computers. J. Geophys. Res., Ocean 102 (C3), 5753–5766.

Mauritzen, C., Rudels, B., Toole, J., 2013. The Arctic and Subarctic Oceans/Seas. International Geophysics Ocean Circulation and Climate - A 21st Century Perspective, pp. 443–470.

Maykut, G.A., Untersteiner, N., 1971. Some results from a time-dependent thermodynamic model of sea ice. J. Geophys. Res. 76 (6), 1550–1575.

Menemenli, D., Hill, C., Adcroft, A., Campin, J., Cheng, B., Ciotti, B., Fukumori, I., Koehl, A., Heimbach, P., Henze, C., Lee, T., Stammer, D., Taft, J., Zhang, J., 2005. Towards eddy permitting estimate of the global ocean and sea-ice circulation. EOS Trans. AGU 86 (9).

Nansen, F., 1902. Oceanography of the North Polar Basin. The Norwegian North Polar Expedition 1896. Scientific Results III (9), 427.

Nguyen, A.T., Woodgate, R., Heimbach, P., 2020. Elucidating large-scale atmospheric controls on Bering Strait throughflow variability using a data-constrained ocean

model and its adjoint. J. Geophys. Res. 125 (9) https://doi.org/10.1029/2020JC016213.
Nguyen, A.T., Pillar, H., Ocaña, A., Bigdeli, V., Smith, T.A., Heimbach, P., 2021. The Arctic Subpolar gyre sTate Estimate (ASTE): Description and assessment of a data-constrained, dynamically consistent ocean-sea ice estimate for 2002–2017. doi: 10.1002/essoar.10504669.1.
Nurser, A.J.G., Bacon, S., 2014. The Rossby radius in the Arctic Ocean. Ocean Sci. 10, 967–975. https://doi.org/10.5194/os-10-967-2014.
Overland, J.E., Wood, K.R., Wang, M., 2011. Warm Arctic- cold continents: climate impacts of the newly open Arctic Sea. Polar Res. 30 (1), 15787. https://doi.org/10.3402/polar.v30i0.15787.
Polyakov, I.V., Timokhov, L.A., Alexeev, V.A., Bacon, S., Dmitrenko, I.A., Fortier, L., Frolov, I.E., Gascard, J.-C., Hansen, E., Ivanov, V.V., Laxon, S., Mauritzen, C., Perovich, D., Shimada, K., Simmons, H.L., Sokolov, V.T., Steele, M., Toole, J., 2010. Arctic ocean warming contributes to reduced polar ice cap. J. Phys. Oceanogr. 40, 2743–2756. https://doi.org/10.1175/2010JPO4339.1.
Polyakov, I.V., Alexeev, V.A., Ashik, I.M., Bacon, S., Beszczynska-Möller, A., Dmitrenko, I., Fortier, L., Gascard, J.-C., Hansen, E., Hölemann, J., Ivanov, V.V., Kikuchi, T., Kirillov, S., Lenn, Y.-D., Piechura, J., Repina, I., Timokhov, L.A., Walczowski, W., Woodgate, R., 2011. Fate of early-2000's Arctic warm water pulse. Bull. Am. Meteorol. Soc. 92 (5), 561–566. https://doi.org/10.1175/2010BAMS2921.1.
Polyakov, I.V., Pnyushkov, A.V., Alkire, M.B., Ashik, I.M., Baumann, T.M., Carmack, E. C., Goszczko, I., Guthrie, J., Ivanov, V.V., Kanzow, T., Krishfield, R., Kwok, R., Sundfjord, A., Morison, J., Rember, R., Yulin, A., 2017. Greater role for Atlantic inflows on sea-ice loss in the Eurasian Basin of the Arctic Ocean. Science 356 (6335), 285–291. https://doi.org/10.1126/science:aai8204.
Proshutinsky, A., Krishfield, R., Toole, J.M., Timmermans, M.-L., Williams, W., Zimmermann, S., Yamamoto-Kawai, M., Armitage, T.W.K., Dukhovskoy, D., Golubeva, E., Manucharyan, G.E., Platov, G., Watanabe, E., Kikuchi, T., Nishino, S., Itoh, M., Kang, S.-H., Cho, K.-H., Tateyama, K., Zhao, J., 2019. Analysis of the Beaufort Gyre freshwater content in 2003–2018. J. Geophys. Res. Oceans 124 (12), 9658–9689. https://doi.org/10.1029/2019JC015281.
Rudels, B., Jones, E.P., Schauer, U., Eriksson, P., 2004. Atlantic sources of the Arctic Ocean surface and halocline waters. Polar Res. 23 (2), 181–208.
Rudels, B., Anderson, L., Eriksson, P., Fahrbach, E., Jakobsson, M., Jones, E., Melling, H., Prinsenberg, S., Schauer, U., Yao, T., 2012. Observations. In: The Ocean, volume 43. Springer Netherlands, pp. 117–498.
Rudels, B., J. Friedrich, H., Quadfasel, D., 1999. The arctic circumpolar boundary current. Deep Sea Res. Part II 46 (6-7), 1023–1062.
Rudels, B., 1989. The formation of polar surface water, the ice export and the exchanges through the Fram Strait. Prog. Oceanogr. 22 (3), 205–248.
Schlitzer, R., 2020. Ocean Data Viewer. odv.awi.de.
Shiklomanov, A.I., Yakovleva, T.I., Lammers, R.B., Karasev, I.P., Vörösmarty, C.J., Linder, E., 2006. Cold region river discharge uncertainty—estimates from large Russian rivers. J. Hydrol. 326 (1-4), 231–256.
Skagseth, O., Furevik, T., Ingvaldsen, R., Loeng, K., Arne, M., Orvik, K., Ozhigin, V., 2008. Volume and heat transports to the Arctic Ocean via the Norwegian and Barents Seas. Arctic-Subarctic Ocean Fluxes, 45–64.
Smith, W.H.F., Sandwell, D.T., 1997. Global sea floor topography from satellite altimetry and ship depth soundings. Science 277 (5334), 1956–1962.
Spall, M., 2013. On the circulation of Atlantic Water in the Arctic Ocean. J. Phys. Oceanogr. 43 (11), 2352–2371.
Steele, M., Boyd, T., 1998. Retreat of the cold halocline layer in the Arctic Ocean. J. Geophys. Res. Oceans 103 (C5), 10419–10435.
Stigebrandt, A., 1981. A Model for the thickness and salinity of the upper layer in the Arctic Ocean and the relationship between the ice thickness and some external parameters. J. Phys. Oceanogr. 11 (10), 1407–1422.
Swift, J.H., Jones, E.P., Aagaard, K., Carmack, E.C., Hingston, M., MacDonald, R.W., McLaughlin, F.A., Perkin, R.G., 1997. Waters of the Makarov and Canada Basins. Deep Sea Res. Part II 44 (8), 1503–1529.
Thyng, K., Greene, C., Hetland, R., Zimmerle, H., DiMarco, S., 2016. True colors of oceanography: Guidelines for effective and accurate colormap selection. Oceanography 29 (3), 9–13. https://doi.org/10.5670/oceanog10.5670/oceanog.2016.66.
Tsubouchi, T., Bacon, S., Naveira Garabato, A.C., Aksenov, Y., Laxon, S.W., Fahrbach, E., Beszczynska-Möller, A., Hansen, E., Lee, C.M., Ingvaldsen, R.B., 2012. The Arctic Ocean in summer: a quasi-synoptic inverse estimate of boundary fluxes and water mass transformation. J. Geophys. Res. 117 (C1) https://doi.org/10.1029/2011JC007174.
Tsubouchi, T., Bacon, S., Aksenov, Y., Naveira Garabato, A.C., Beszczynska-Möller, A., Hansen, E., de Steur, L., Curry, B., Lee, C.M., 2018. The Arctic Ocean seasonal cycles of heat and freshwater fluxes: observation-based inverse estimates. J. Phys. Oceanogr. 48, 2029–2055. https://doi.org/10.1175/JPO-D-17-0239.1.
Tsubouchi, T., von Appen, W.-J., Schauer, U., Kanzow, T., Lee, C., Curry, B., de Steur, L., Ingvaldsen, R., Woodgate, R.A., 2019. The Arctic Ocean volume, heat and fresh water transports time series from October 2004 to May 2010. PANGAEA. https://doi.org/10.1594/PANGAEA.909966.
Tsubouchi, T., Våge, K., Hansen, B., Margretha, K., Larsen, H., Østerhus, S., Johnson, C., Jónsson, S., Valdimarsson, H., 2021. Increased ocean heat transport into the Nordic Seas and Arctic Ocean over the period 1993–2016 Nature. Clim. Change 11, 21–26. https://doi.org/10.1038/s41558-020-00941-3.
Timmermans, M.-L., Marshall, J., 2020. Understanding Arctic Ocean circulation: A review of ocean dynamics in a changing climate. J. Geophys. Res.: Oceans, 125, e2018JC014378. https://doi.org/10.1029/2018JC014378.
Toole, J., Krishfield, R., Timmermans, M.-L., Proshutinsky, A., 2011. The ice-tethered profiler: Argo of the arctic. Oceanography 24 (3), 126–135.
Woodgate, R.A., Aagaard, K., Muench, R.D., Gunn, J., Bjork, G., Rudels, B., Roach, A.T., Schauer, U., 2001. The Arctic Ocean Boundary Current along the Eurasian slope and the adjacent Lomonosov Ridge: watermass properties, transports and transformations from moored instruments. Deep Sea Res. Part I 48, 1757–1792. https://doi.org/10.1016/S0967-0637(00)00091-1.
Woodgate, R.A., 2018. Increases in the Pacific inflow to the Arctic from 1990 to 2015, and insights into seasonal trends and driving mechanisms from year-round Bering Strait mooring data. Prog. Oceanogr. 160, 124–154.
Wunsch, C., Heimbach, P., 2007. Practical global oceanic state estimation. Physica D 230 (1-2), 197–208.
Zhang, J., Rothrock, D.A., 2003. Modeling global sea ice with a thickness and enthalpy distribution model in generalized curvilinear coordinates. Mon. Wea. Rev. 131 (5), 845–861.
Zhao, M., Timmermans, M.-L., Cole, S., Krishfield, R., Proshutinsky, A., Toole, J., 2014. Characterizing the eddy field in the Arctic Ocean halocline. J. Geophys. Res. Oceans 119 (12), 8800–8817. https://doi.org/10.1002/2014JC010488.
Zhong, W., Steele, M., Zhang, J., Cole, S.T., 2019. Circulation of Pacific Winter Water in the Western Arctic Ocean. J. Geophys. Res. Oceans 124 (2), 863–881. https://doi.org/10.1029/2018JC014604.